



Calhoun: The NPS Institutional Archive
DSpace Repository

Theses and Dissertations

1. Thesis and Dissertation Collection, all items

2016-06

Development of improved design and 3D printing manufacture of cross-flow fan rotor

Waterman, Timothy J.

Monterey, California: Naval Postgraduate School

<http://hdl.handle.net/10945/49411>

Downloaded from NPS Archive: Calhoun



Calhoun is a project of the Dudley Knox Library at NPS, furthering the precepts and goals of open government and government transparency. All information contained herein has been approved for release by the NPS Public Affairs Officer.

Dudley Knox Library / Naval Postgraduate School
411 Dyer Road / 1 University Circle
Monterey, California USA 93943

<http://www.nps.edu/library>



**NAVAL
POSTGRADUATE
SCHOOL**

MONTEREY, CALIFORNIA

THESIS

**DEVELOPMENT OF IMPROVED DESIGN AND 3D
PRINTING MANUFACTURE OF CROSS-FLOW FAN
ROTOR**

by

Timothy J. Waterman

June 2016

Thesis Advisor:
Co-Advisor:

Garth V. Hobson
Anthony J. Gannon

Approved for public release; distribution is unlimited

THIS PAGE INTENTIONALLY LEFT BLANK

REPORT DOCUMENTATION PAGE			Form Approved OMB No. 0704-0188	
Public reporting burden for this collection of information is estimated to average 1 hour per response, including the time for reviewing instruction, searching existing data sources, gathering and maintaining the data needed, and completing and reviewing the collection of information. Send comments regarding this burden estimate or any other aspect of this collection of information, including suggestions for reducing this burden, to Washington headquarters Services, Directorate for Information Operations and Reports, 1215 Jefferson Davis Highway, Suite 1204, Arlington, VA 22202-4302, and to the Office of Management and Budget, Paperwork Reduction Project (0704-0188) Washington, DC 20503.				
1. AGENCY USE ONLY (Leave blank)	2. REPORT DATE June 2016	3. REPORT TYPE AND DATES COVERED Master's thesis		
4. TITLE AND SUBTITLE DEVELOPMENT OF IMPROVED DESIGN AND 3D PRINTING MANUFACTURE OF CROSS-FLOW FAN ROTOR			5. FUNDING NUMBERS	
6. AUTHOR(S) Timothy J. Waterman				
7. PERFORMING ORGANIZATION NAME(S) AND ADDRESS(ES) Naval Postgraduate School Monterey, CA 93943-5000			8. PERFORMING ORGANIZATION REPORT NUMBER	
9. SPONSORING /MONITORING AGENCY NAME(S) AND ADDRESS(ES) TDSI-National University of Singapore 21 Lower Kent Ridge Road Singapore, 119077			10. SPONSORING / MONITORING AGENCY REPORT NUMBER	
11. SUPPLEMENTARY NOTES The views expressed in this thesis are those of the author and do not reflect the official policy or position of the Department of Defense or the U.S. Government. IRB Protocol number ____N/A____.				
12a. DISTRIBUTION / AVAILABILITY STATEMENT Approved for public release; distribution is unlimited			12b. DISTRIBUTION CODE A	
13. ABSTRACT (maximum 200 words) This study determined the optimum blade stagger angle for a cross-flow fan rotor and evaluated the performance of a 3D printed rotor. Using ANSYS-CFX and SolidWorks, the cross-flow fan was modeled computationally and tested at 8,000 rpm. A parametric study determined optimum blade stagger angle using thrust, power, and thrust-to-power ratio as desired output variables. A MarkForged Mark One 3D printer was used to print components of a carbon-fiber composite cross-flow fan rotor. These pieces were assembled and the thrust, power, and thrust-to-power ratio of the 3D printed rotor were measured. These performance characteristics were compared to a rotor of the same geometry previously manufactured from traditional carbon fiber components. The optimum stagger angle for the current 26-bladed, 101.6 mm (4 inch) diameter rotor was determined to be 10° forward of its previous position. The 3D printed rotor was found to produce less thrust, but also required less power. This was thought to be caused by the outward deflection of the rotor blades due to centripetal force in conjunction with the surface roughness of the blades. The rotor did have a similar thrust-to-power ratio as the current cross-flow fan rotor at speeds of up to 8,000 rpm.				
14. SUBJECT TERMS cross-flow fan, vertical take-off and landing, 3D printing, computational fluid dynamics, VTOL, CFD			15. NUMBER OF PAGES 77	
			16. PRICE CODE	
17. SECURITY CLASSIFICATION OF REPORT Unclassified	18. SECURITY CLASSIFICATION OF THIS PAGE Unclassified	19. SECURITY CLASSIFICATION OF ABSTRACT Unclassified	20. LIMITATION OF ABSTRACT UU	

THIS PAGE INTENTIONALLY LEFT BLANK

Approved for public release; distribution is unlimited

**DEVELOPMENT OF IMPROVED DESIGN AND 3D PRINTING
MANUFACTURE OF CROSS-FLOW FAN ROTOR**

Timothy J. Waterman
Ensign, United States Navy
B.S., United States Naval Academy, 2015

Submitted in partial fulfillment of the
requirements for the degree of

MASTER OF SCIENCE IN MECHANICAL ENGINEERING

from the

**NAVAL POSTGRADUATE SCHOOL
June 2016**

Approved by: Garth V. Hobson
Thesis Advisor

Anthony J. Gannon
Co-Advisor

Garth V. Hobson
Chair, Department of Mechanical and Aerospace Engineering

THIS PAGE INTENTIONALLY LEFT BLANK

ABSTRACT

This study determined the optimum blade stagger angle for a cross-flow fan rotor and evaluated the performance of a 3D printed rotor. Using ANSYS-CFX and SolidWorks, the cross-flow fan was modeled computationally and tested at 8,000 rpm. A parametric study determined optimum blade stagger angle using thrust, power, and thrust-to-power ratio as desired output variables. A MarkForged Mark One 3D printer was used to print components of a carbon-fiber composite cross-flow fan rotor. These pieces were assembled and the thrust, power, and thrust-to-power ratio of the 3D printed rotor were measured. These performance characteristics were compared to a rotor of the same geometry previously manufactured from traditional carbon fiber components. The optimum stagger angle for the current 26-bladed, 101.6 mm (4 inch) diameter rotor was determined to be 10° forward of its previous position. The 3D printed rotor was found to produce less thrust, but also required less power. This was thought to be caused by the outward deflection of the rotor blades due to centripetal force in conjunction with the surface roughness of the blades. The rotor did have a similar thrust-to-power ratio as the current cross-flow fan rotor at speeds of up to 8,000 rpm.

THIS PAGE INTENTIONALLY LEFT BLANK

TABLE OF CONTENTS

I.	INTRODUCTION.....	1
II.	PARAMETRIC STUDY OF CROSS-FLOW FAN BLADE STAGGER AND SHAPE.....	5
	A. MODELING SETUP	6
	B. BLADE STAGGER ANGLE DESIGN STUDY SETUP	7
	C. MESHING	9
	D. BOUNDARY CONDITIONS.....	11
	E. SIMULATION	13
III.	3D PRINTING OF CROSS-FLOW FAN AND EXPERIMENTAL SETUP.....	15
	A. 3D PRINTING METHODS	15
	1. 3D Printing Capabilities and Limitations.....	15
	2. Solid Modeling.....	17
	B. FABRICATION OF 3D PRINTED ROTOR.....	18
	1. Printing Process	18
	2. Assembly of Rotor.....	20
	C. EXPERIMENTAL SETUP	22
	1. Testing Apparatus.....	22
	2. Data Acquisition.....	24
IV.	RESULTS AND DISCUSSION	27
	A. MODEL CONVERGENCE.....	27
	B. FLOW VISUALIZATION.....	28
	C. DESIGN STUDY RESULTS	30
	1. Thrust.....	30
	2. Power.....	31
	3. Efficiency	32
	D. COMPARISON OF EXPERIMENTAL RESULTS FOR EXISTING DESIGN AND 3D PRINTED DESIGN.....	34
	1. Thrust.....	35
	2. Power.....	36
	3. Thrust-to-Power Ratio.....	37
	E. 3D PRINTING LIMITATIONS	37

V.	CONCLUSIONS	41
A.	OPTIMUM STAGGER ANGLE	41
B.	VIABILITY OF 3D PRINTED CROSS-FLOW FAN ROTOR.....	41
C.	RECOMMENDATIONS.....	42
APPENDIX A. DIMENSIONED DRAWINGS OF COMPUTATIONAL DOMAINS		43
APPENDIX B. CFX INPUT FILE SETTINGS		45
APPENDIX C. DIMENSIONED DRAWINGS OF 3D PRINTER INPUT FILES.....		57
LIST OF REFERENCES		59
INITIAL DISTRIBUTION LIST		61

LIST OF FIGURES

Figure 1.	Original cross-flow fan design as patented by Mortier. Source: [1].	1
Figure 2.	UAV built by Jones. Source: [5].	2
Figure 3.	CFF UAV designed and successfully flown by Smitley. Source: [7].	3
Figure 4.	SolidWorks model of a 26-bladed CFF rotor. Source: [6].	6
Figure 5.	SolidWorks model of the CFF housing. Source: [6].	6
Figure 6.	Complete rotor assembly geometry in DesignModeler. Source: [6].	7
Figure 7.	Positive and negative stagger angles.	8
Figure 8.	Blade stagger angle as measured from the X-axis.	8
Figure 9.	Plus five degree stagger angle sketch.	9
Figure 10.	Minus five degree stagger angle sketch.	9
Figure 11.	Mesh of baseline model for design study.	10
Figure 12.	Edge sizing along housing-rotor interface and perimeter of rotor blades.	11
Figure 13.	Boundary conditions of design studies.	12
Figure 14.	The MarkForged Mark One.	16
Figure 15.	MarkForged Mark One nozzles.	16
Figure 16.	Solid model for 3D printer of rotor endcap.	17
Figure 17.	Solid model for 3D printer of rotor blades.	18
Figure 18.	Eiger model of rotor endcap detailing fiber placement.	19
Figure 19.	Eiger model of rotor blade detailing fiber placement.	19
Figure 20.	Partially assembled 3D printed CFF rotor in lathe jig.	20
Figure 21.	Detail of 3D printed CFF rotor blades bonded to endcap.	21
Figure 22.	Fully assembled 3D printed CFF rotor.	21

Figure 23.	Complete CFF assembly with 3D printed rotor.	22
Figure 24.	Full CFF thrust and power testing experimental setup.	22
Figure 25.	Control panel for manual input to CFF speed controller.	23
Figure 26.	Stroboscope used to measure rotational speed of CFF rotor.	24
Figure 27.	Clamp ammeter measuring current to motor from battery.	25
Figure 28.	Electronic balance used to measure CFF thrust.	25
Figure 29.	Mass flows and rotor torque over simulation duration for baseline model simulation at 8,000 rpm.	27
Figure 30.	Baseline model velocity streamlines at 8,000 rpm.	28
Figure 31.	Baseline model pressure field at 8,000 rpm.	29
Figure 32.	Thrust as a function of stagger angle.	31
Figure 33.	Power as a function of stagger angle.	32
Figure 34.	Isentropic efficiency as a function of stagger angle.	33
Figure 35.	Thrust-to-power ratio as a function of stagger angle.	33
Figure 36.	Thrust output of existing and 3D printed CFF rotor. Some CFX model data from Martin [6].	35
Figure 37.	Power output of existing and 3D printed CFF rotor. Some CFX model data from Martin [6].	36
Figure 38.	Thrust-to-power ratio for existing and 3D printed CFF rotors. CFX model data from Martin [6].	37
Figure 39.	Surface roughness on the pressure side of 3D printed rotor blade.	38
Figure 40.	Schematic of printed blade profile overlaid on profile of printer input file.	38

LIST OF TABLES

Table 1. Thrust-to-weight ratio for 3D printed rotor and existing rotor.41

THIS PAGE INTENTIONALLY LEFT BLANK

ACKNOWLEDGMENTS

The author would like to acknowledge the following people:

Dr. Garth Hobson, for his technical advice and extensive knowledge of computational fluid dynamics.

Dr. Anthony Gannon, for his troubleshooting abilities.

John Gibson, for his uncanny knack for getting anything and everything working again.

THIS PAGE INTENTIONALLY LEFT BLANK

I. INTRODUCTION

The cross-flow fan (CFF) was first patented in the U.S. in 1893 by Mortier. Figure 1 shows the original patent design.

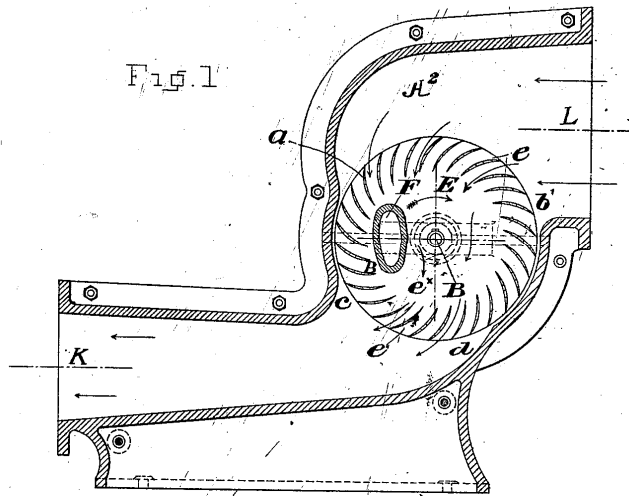


Figure 1. Original cross-flow fan design as patented by Mortier. Source: [1].

Since then, many applications of CFFs have emerged. The U.S. Department of Defense considered cross-flow fans for aircraft propulsion as early as 1969, when a U.S. Army survey of propulsion methods for horizontal-axis rotating wing aeronautical systems included the cross-flow fan embedded in a wing [2]. In 1975, the U.S. Navy awarded a contract to Vought Systems Division to explore the CFF as a method of aircraft propulsion [3]. Further investigation of the CFF continued in the 1980s with the advent of computational fluid dynamics (CFD). Harloff and Wilson in 1981 examined a cross-flow fan using CFD methods and determined that housing shape vastly affected the fan performance, including when embedding the fan in a wing [4]. Recently, CFFs have emerged as a candidate for next-generation vertical take-off and landing (VTOL) aircraft propulsion and continue to be investigated by the U.S. Navy through research done at the Naval Postgraduate School (NPS). Specifically, Jones, Martin, and Smitley have recently

done studies at NPS examining the applicability of CFFs for the propulsion of small unmanned aerial vehicles (UAVs) [5]–[7].

The studies undertaken at NPS have focused on the viability and performance of CFFs as a method of propulsion. Jones first achieved vertical tethered flight with a 4-rotor UAV powered by two electric motors [5]. Figure 2 shows Jones' UAV.



Figure 2. UAV built by Jones. Source: [5].

This UAV proved that cross-flow fans were capable of powering a system with a thrust to weight ratio greater than one. Martin, using the CFF rotors from Jones, subjected the design to studies varying the number of blades on a 101.6 mm (4 inch) diameter CFF rotor. He concluded by use of numerical simulations that the optimal number of blades for that rotor design was 26. Martin then manufactured three rotors and experimentally verified his CFD calculations, proving that the 26-bladed design was superior [6]. Much of Martin's work was the basis of this study. Finally, Smitley, using the rotors designed by Martin, manufactured a CFF-powered UAV that achieved untethered stable flight [7]. This UAV is pictured in Figure 3.

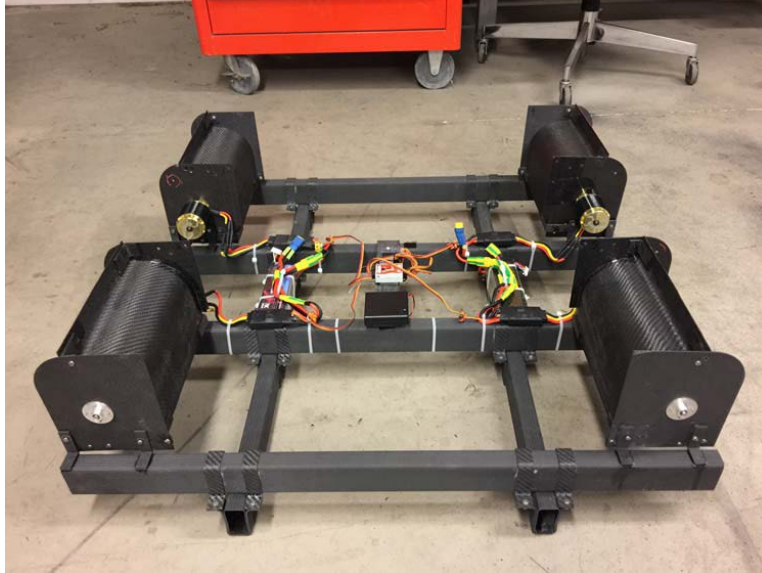


Figure 3. CFF UAV designed and successfully flown by Smitley. Source: [7].

Since a CFF UAV had proven to be feasible, the logical next step was to find ways to improve the performance of the UAV. One easily identifiable area of improvement was fan design. Although Martin undertook a study of the blade number, no study at NPS had yet examined the shape of the blade or the blade orientation on the rotor. Yao did perform a design optimization of CFF rotor blades and concluded that the blade shape and stagger angle should be changed [8]. However, Yao's results were unable to be replicated using ANSYS-CFX. Examining the blade stagger angle instead of blade shape was determined to be more practical. Besides the blade stagger angle, the manufacturing method of the rotor could also be changed. New 3D printing technology, in particular the MarkForged Mark One carbon fiber 3D printer, for the first time now allowed fully composite parts to be 3D printed. This technology showed promise in rapidly manufacturing complicated blade and rotor geometries.

The objective of this study was twofold. First was to further improve the performance characteristics of the cross-flow fan rotor through a design study incorporating blade stagger angle. Second was to manufacture by 3D printing using the MarkForged Mark One a carbon-fiber composite rotor and compare its performance characteristics to the existing design.

THIS PAGE INTENTIONALLY LEFT BLANK

II. PARAMETRIC STUDY OF CROSS-FLOW FAN BLADE STAGGER AND SHAPE

Computational optimization work done by Martin [6] determined that the optimal number of blades for the chosen cross-flow fan geometry operating at 8,000 rpm is 26. Martin was able to experimentally validate his simulations, but at a fan rotor speed of only 7,000 rpm. This work was taken to be the baseline model. In an effort to further increase thrust, power output, and efficiency over Martin's baseline model the stagger angle was also examined. All studies used ANSYS-CFX. Blade stagger angles -5, 0, 3, 5, 7, 10, and 15 degrees relative to the current position were simulated. Using commercial solid modeling software SolidWorks, 2D models were generated, then imported into ANSYS-CFX. The fluid domain geometry was split into two parts, the stationary housing and the spinning rotor. A sliding mesh connection was used between the rotor and housing domains. Using a fine mesh of approximately 100,000 elements, as well as specifying the number of elements along the rotor-housing interface, ensured sufficient data resolution for valid results.

A. MODELING SETUP

Martin's original geometry is shown in Figures 4 and 5.

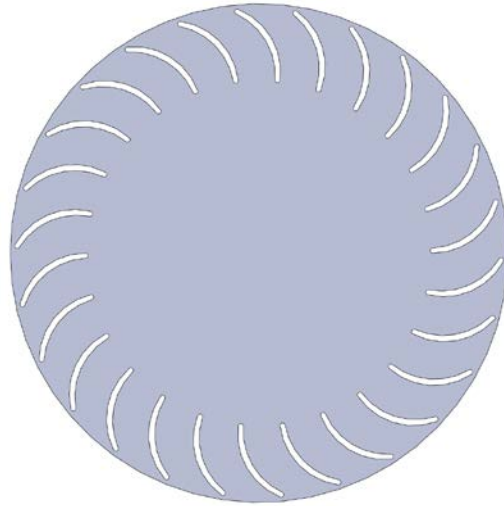


Figure 4. SolidWorks model of a 26-bladed CFF rotor. Source: [6].

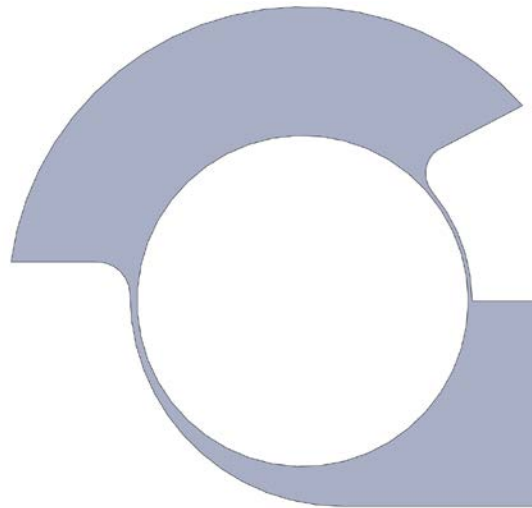


Figure 5. SolidWorks model of the CFF housing. Source: [6].

Because ANSYS-CFX interprets solid objects as fluid domains, the drawings shown are in fact negatives of the real parts. Using sketch tools, a 2D design was drawn, then extruded to a thickness of 1 mm. Complete dimensioned drawings are in Appendix A. Each part was imported separately into CFX's DesignModeler. The complete assembly in DesignModeler is shown in Figure 6.

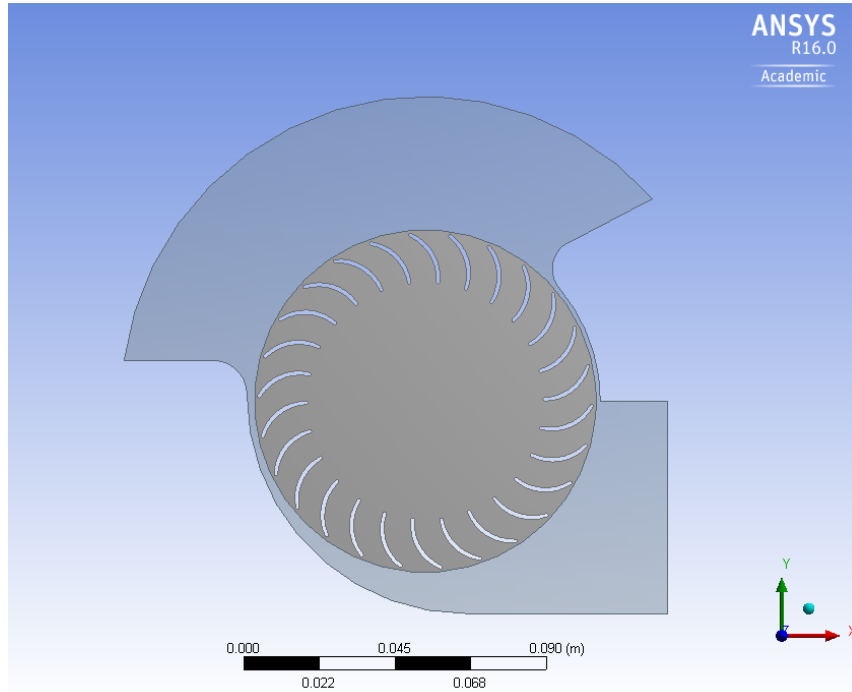


Figure 6. Complete rotor assembly geometry in DesignModeler. Source: [6].

B. BLADE STAGGER ANGLE DESIGN STUDY SETUP

Blade stagger angle describes the orientation angle of the airfoil with respect to the rotor. For this study, positive stagger angle was defined as rotating away from the X-axis and negative stagger was defined as rotating toward it. Figure 7 illustrates a positive and negative stagger angle blade position relative to both the baseline configuration and the X-axis.

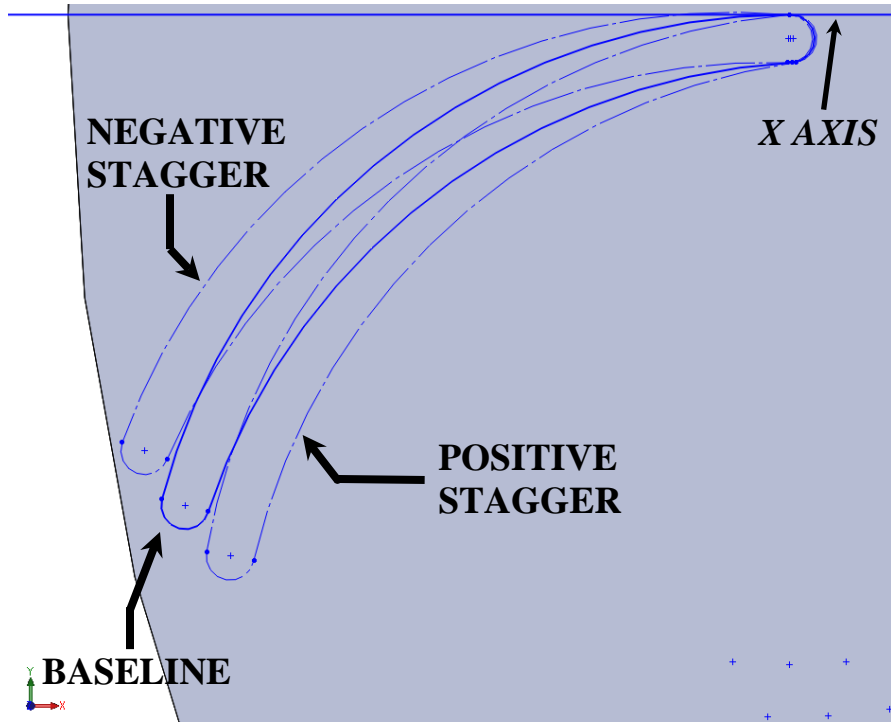


Figure 7. Positive and negative stagger angles.

Figure 8 shows the blade stagger angle of the original design as measured from the X-axis.

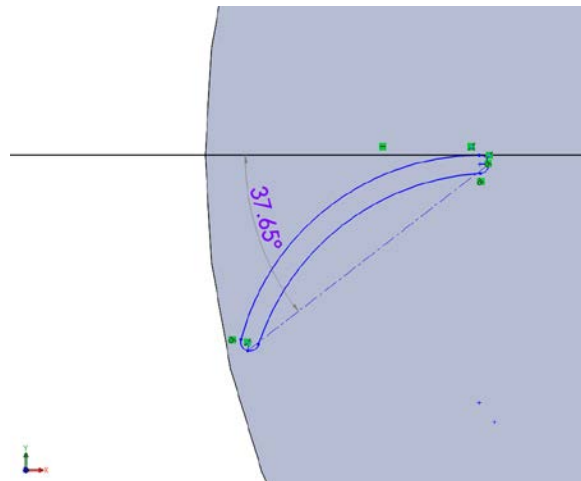


Figure 8. Blade stagger angle as measured from the X-axis.

This position is zero stagger angle, as it is the reference for the rest of the design study. The geometry was modified to decrease the stagger angle by five degrees and increase it by 3, 5, 7, 10, and 15 degrees. Figure 9 shows the plus five and Figure 10 shows the minus five degree stagger angle sketches in SolidWorks.

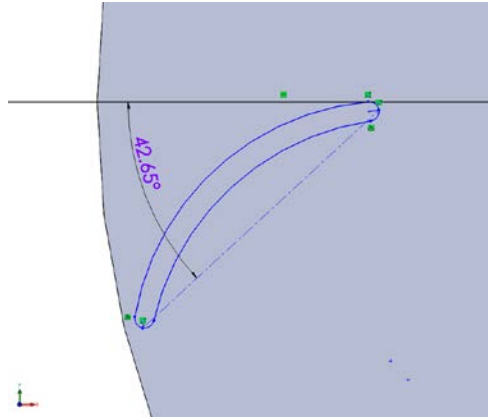


Figure 9. Plus five degree stagger angle sketch.

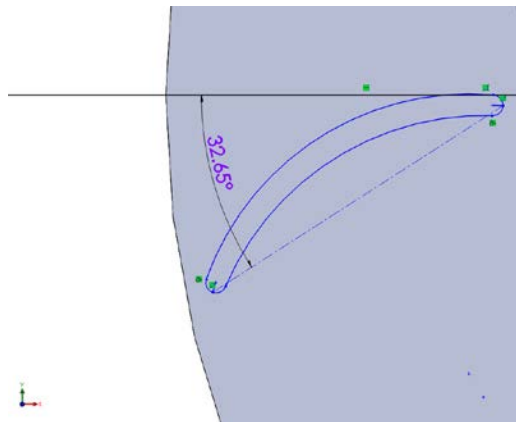


Figure 10. Minus five degree stagger angle sketch.

C. MESHING

After the SolidWorks model was converted to a DesignModeler geometry, ANSYS-CFX was used to mesh the part. CFX created a fine mesh with over 93,000 nodes and 43,000 elements. Figure 11 shows the mesh of the baseline model.

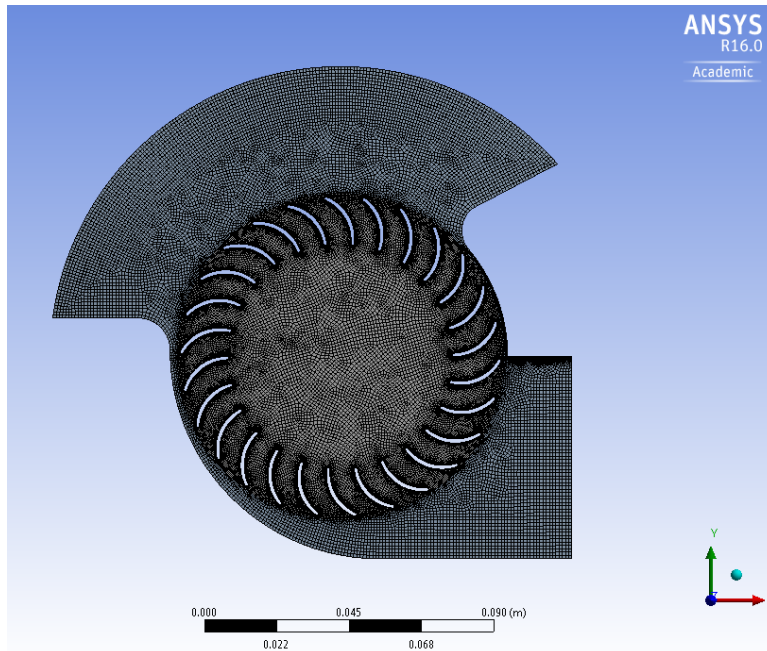


Figure 11. Mesh of baseline model for design study.

A sweep method was implemented which forced the element width of the domain to be one, creating a quasi-2D domain. An edge sizing specification on the interface between the housing and the rotor ensured that both had the same number of elements along the interface. Additionally, edge refinements were also specified around each blade in order to accurately capture the flow characteristics along the surface of the blades. Figure 12 shows the edge refinement around a rotor blade, as well as the edge sizing on the housing-rotor interface.

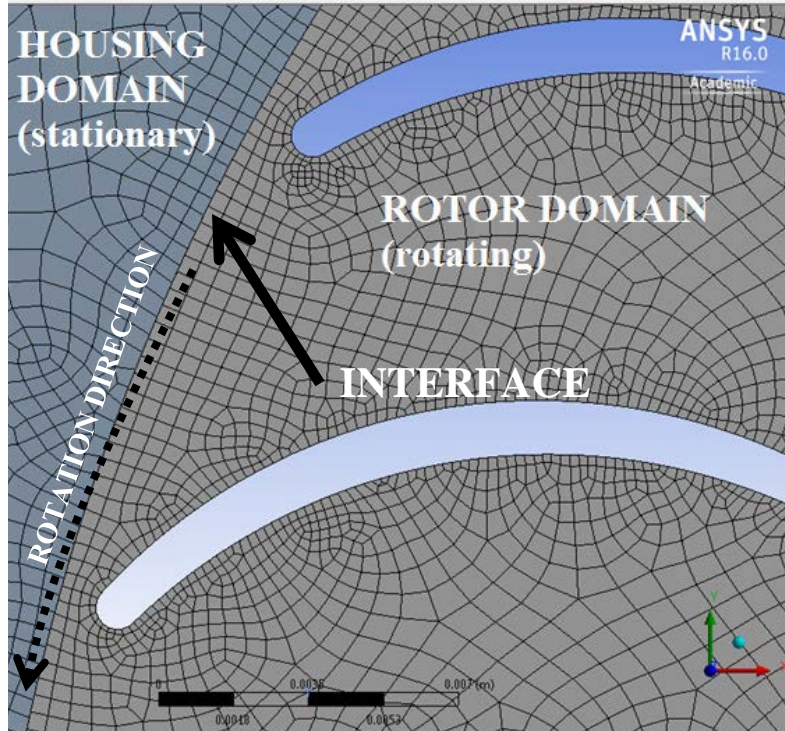


Figure 12. Edge sizing along housing-rotor interface and perimeter of rotor blades.

D. BOUNDARY CONDITIONS

Each design study had the same basic geometry, except the blade position, and therefore each had the same boundary conditions. The boundary conditions for the baseline design model are shown in Figure 13. Note that the upper and lower housing boundaries are defined due to their orientation on the actual assembly, not the model geometry.

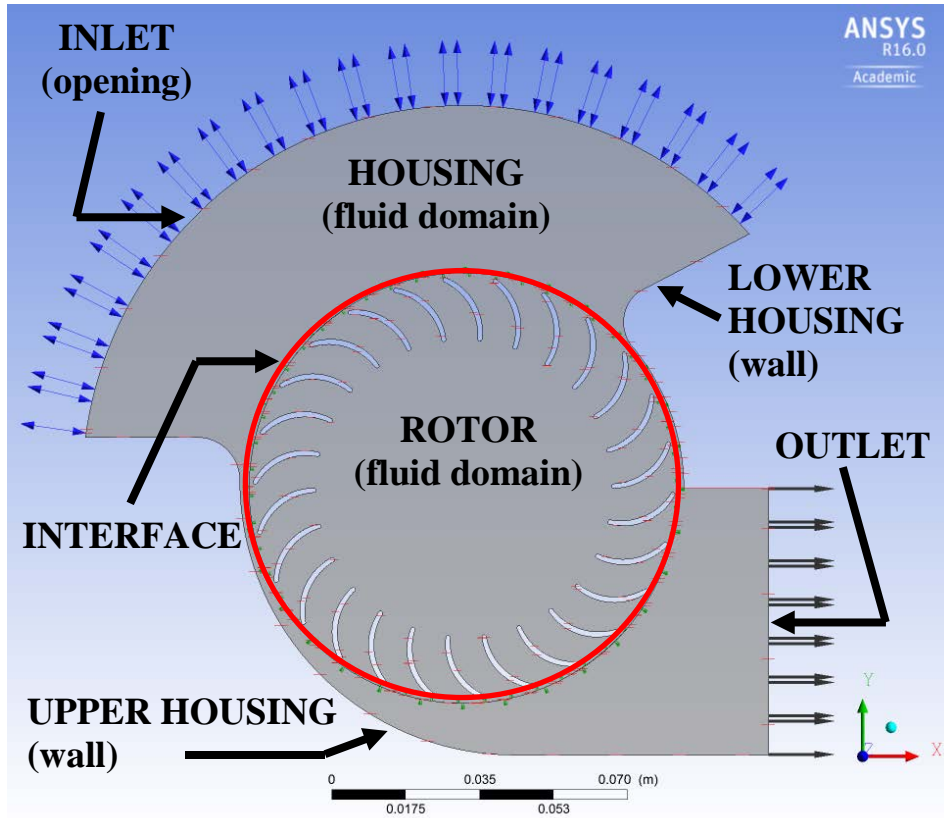


Figure 13. Boundary conditions of design studies.

The inlet boundary condition was defined as an opening, meaning that flow could both enter and exit at this boundary. The outlet flow was fixed as only being allowed to exit. Having both boundaries as openings, though it mimics reality, would open up the possibility of pressure oscillations pulsing in and out of both ends. All walls were set as no-slip adiabatic boundaries. Based on previous work done by Martin, running a transient simulation for a total time of 0.0375 s was the most appropriate time to allow the flow field to develop fully through the rotor [6]. The time step was fixed at a value equivalent to one degree of rotation, and as also previously proved by Martin, this value is adequate to accurately simulate the flow [6]. CFX used a second-order backwards Euler differencing scheme to solve the equations of fluid flow. The fluid was air as an ideal gas with the total energy fluid domain option invoked. The k-Epsilon turbulence model was implemented in all simulations. Full details of the ANSYS-CFX setup file can be found in Appendix B.

E. SIMULATION

Since transient simulations were used throughout the design study, each solver run was monitored. Plotting the value of the mass flows, as well as the torque on the rotor blades, allowed a simple method of determining whether or not the solution had reached steady-state oscillation. Accurately determining the worth of a design requires the collection of data relevant to a number of performance parameters. Of most interest are the thrust and power data. The optimum design maximizes thrust while minimizing power consumed. Thrust can be calculated from the mass flow data, while torque is used to calculate the power absorbed the by the rotor. In this way, performance can be compared among different blade angles and rotor speeds.

THIS PAGE INTENTIONALLY LEFT BLANK

III. 3D PRINTING OF CROSS-FLOW FAN AND EXPERIMENTAL SETUP

The previous rotor design for the CFF UAV was manufactured using custom-made carbon fiber parts. While the design is robust and effective, rapid prototyping of new designs is both prohibitively expensive and time consuming. 3D printing offers a viable alternative to traditional machining and forming. The MarkForged Mark One 3D printer is capable of 3D printing a nylon-carbon fiber composite, and thus was a suitable choice for the manufacture of a new rotor. The objective was to manufacture a rotor from 3D printed carbon fiber parts and determine its performance. In this way, future design changes can be made to the rotor in a rapid manner and manufactured natively. In order to compare this 3D printed rotor to the current rotors, the experimental setup from Martin [6] was replicated in order to enable direct comparison of performance between the rotors.

A. 3D PRINTING METHODS

1. 3D Printing Capabilities and Limitations

In order to understand design choices made in the manufacturing of this rotor, it is necessary to understand how the MarkForged Mark One, shown in Figure 14, creates carbon fiber composites.

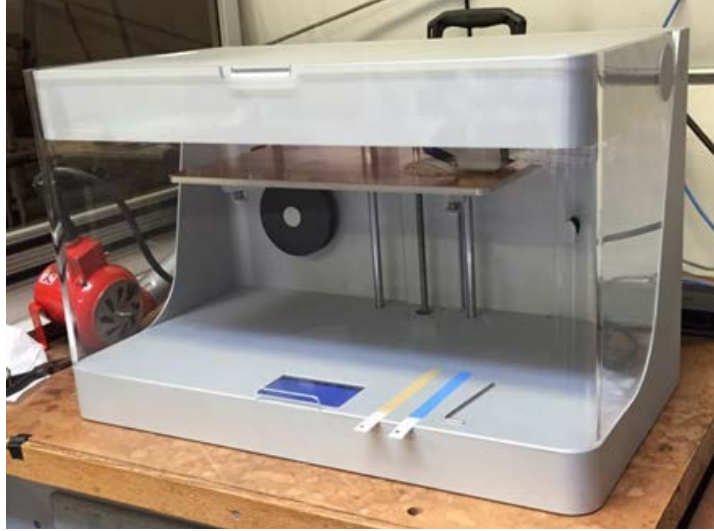


Figure 14. The MarkForged Mark One.

The printer uses two nozzles fed from two different spools. Figure 15 shows the nozzles.

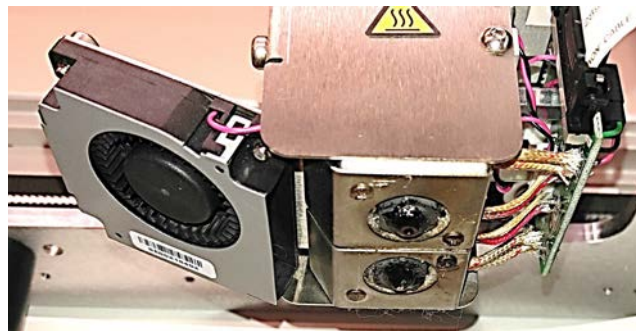


Figure 15. MarkForged Mark One nozzles.

One nozzle lays molten nylon onto the print bed to create the walls, base, and roof of the part. Nylon is also used as fill, or where carbon fiber will not fit into the part. The second nozzle lays down a continuous strand of carbon fiber that deforms when passed through the heated fiber nozzle. In this way, the printer can lay fiber around corners in one continuous strand. However, this places limitations on where the printer can place fiber. First, when breaking the part up into horizontal slices, the slicing software determines whether or not there is enough area in each slice to fit fiber. There is no way

to force the software to lay down carbon fiber in a certain area. Also, the fiber spreads out when it melts into the part. This imposes a minimum thickness requirement on parts to contain carbon fiber. Lastly, the fiber cannot be laid down through a tight corner without breaking. Sharp corners or points in any part printed with the Mark One cannot contain fiber.

2. Solid Modeling

The Mark One cannot print the entire rotor at once, for all three reasons given in the previous section. Thus, the rotor was split into two parts: the blades and the endcaps. Solid models were constructed in SolidWorks. These blades and endcaps would then be assembled using techniques first performed by Martin [6]. Figure 16 shows the solid model of the end cap and Figure 17 shows the solid model of the blade.

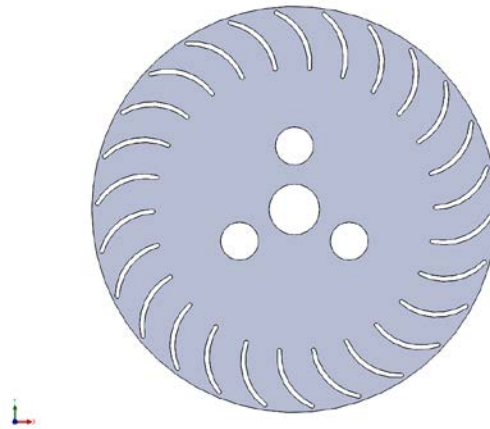


Figure 16. Solid model for 3D printer of rotor endcap.

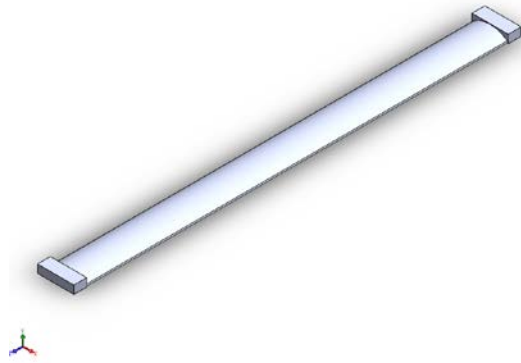


Figure 17. Solid model for 3D printer of rotor blades.

The rotor was 101.6 mm (4 in) in diameter and had 26 blades, and the blades were 208.28 mm (8.2 in) long. Fully dimensioned solid models of the printer input files are found in Appendix C. The rotor manufactured by Martin had a 203.2 mm (8 in) span. In order to account for manufacturing variations, the blades were designed to be slightly longer than 203.3 mm (8 in) with the intention of being cut down to size when assembling the rotor. Furthermore, this enabled the blade to be attached to the end discs by melting the excess nylon on the end of the blade into the nylon of the end disc, which eliminated the need for glue. The endcaps on the rotor also created more surface area per slice in the rotor while eliminating some sharp corners. This increased the amount of carbon fiber that the slicing software could fit into the part.

B. FABRICATION OF 3D PRINTED ROTOR

1. Printing Process

The MarkForged Mark One was controlled through Google Chrome-based software called Eiger. Eiger also contained the slicing and pathing algorithms for the printer. After the solid models were drawn in SolidWorks, they were imported into Eiger as an STL file. Eiger allowed some user control of fill patterns, fill density, and fiber placement. Figure 18 shows the internal view of the rotor endcap created in Eiger.

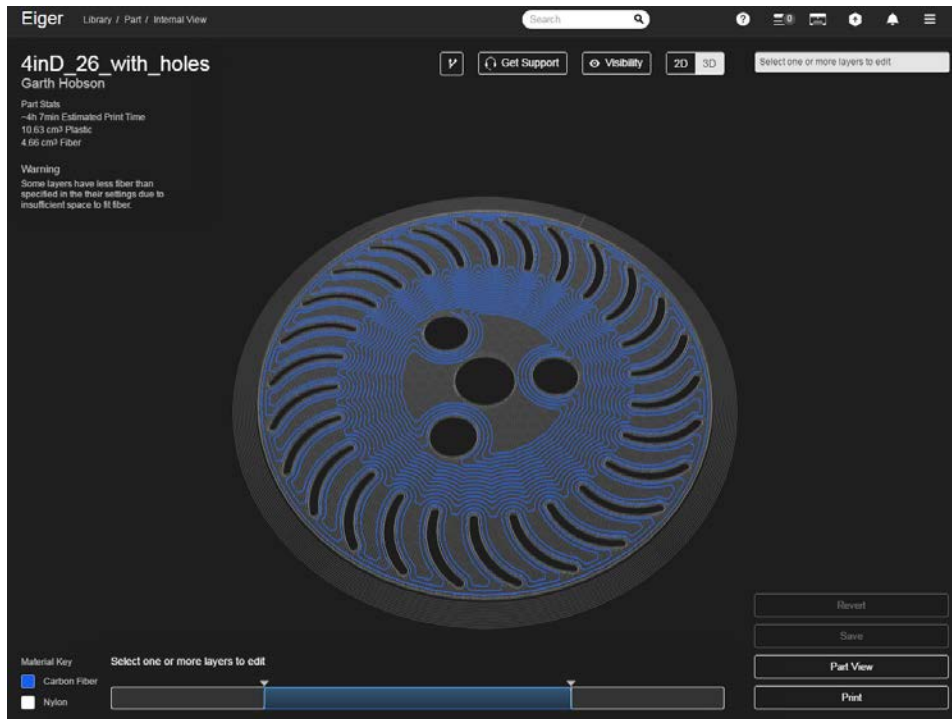


Figure 18. Eiger model of rotor endcap detailing fiber placement.

The bottom of Figure 18 shows the bar detailing where fiber was placed in the part. To prevent printer jams, the fiber was placed halfway through the part. The program took these settings and exported them directly to the Mark One, which then printed the parts. Figure 19 shows a detail of the Eiger model of the rotor blade.

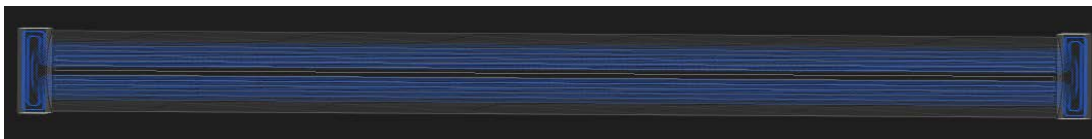


Figure 19. Eiger model of rotor blade detailing fiber placement.

The square endcaps allowed the printer to place more fiber in that slice of the rotor blade because of the extra area. Thus, the amount of fiber in the blade was increased, which increased the stiffness of the blade.

2. Assembly of Rotor

The rotor was assembled using methods similar to Martin [6] in order to maximize the similarity of the rotors. The blades were weighed using a balance, then arranged from lightest to heaviest. A jig was then used to align the endcaps. A third endcap was placed in the middle of the rotor for increased stability and to prevent the blades from excessive flexing due to centripetal forces. This design also mimicked Martin's rotor. The blades were inserted into the endcaps by weight, with blades of similar weight set 180° apart. Using a lathe, the jig was spun after every blade attachment to ensure alignment. The jig is shown in Figure 20.

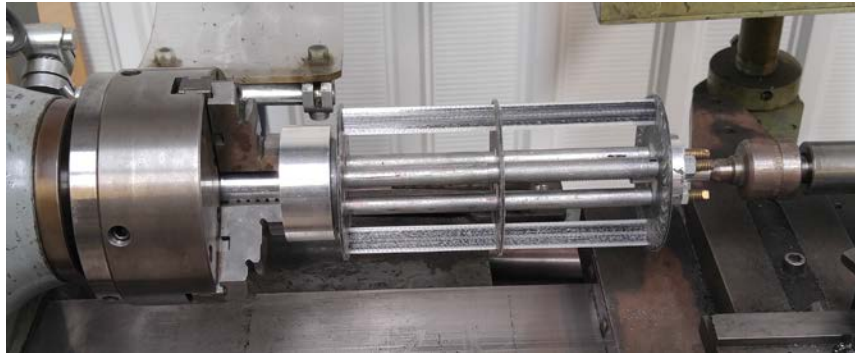


Figure 20. Partially assembled 3D printed CFF rotor in lathe jig.

Using a soldering gun, the ends of the blades were melted into the endcaps, completing the assembly. Lastly, aluminum flanges were attached to the end of the rotor, allowing it to be fixed to the motor shaft and bearing on the housing assembly. A detail of the endcap is shown in Figure 21.



Figure 21. Detail of 3D printed CFF rotor blades bonded to endcap.

Figure 22 shows the assembled rotor.

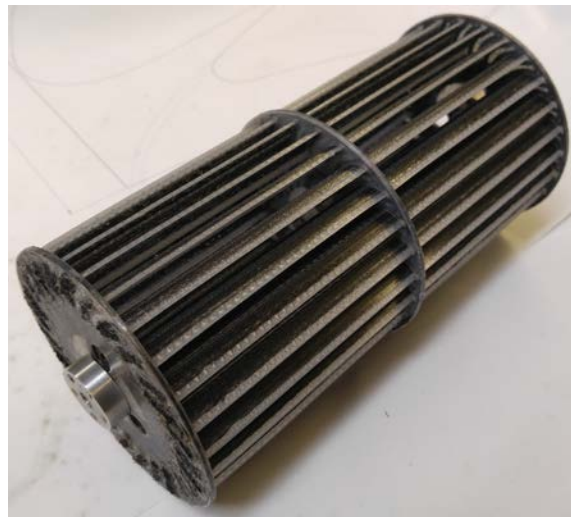


Figure 22. Fully assembled 3D printed CFF rotor.

The rotor was then fastened into the housing built by Martin, shown in Figure 23 [6].



Figure 23. Complete CFF assembly with 3D printed rotor.

C. EXPERIMENTAL SETUP

1. Testing Apparatus

The CFF performance characteristics were measured using the same experimental setup used by Martin [6]. The rotor was placed in a housing manufactured by Martin. Thrust produced was measured by a digital scale with a plate placed on top of it to ensure that the force from the entire exhaust jet was captured. Power absorbed by the fan was measured by an ammeter from the battery and a voltmeter across the battery. Figure 24 shows an overview of the testing setup.

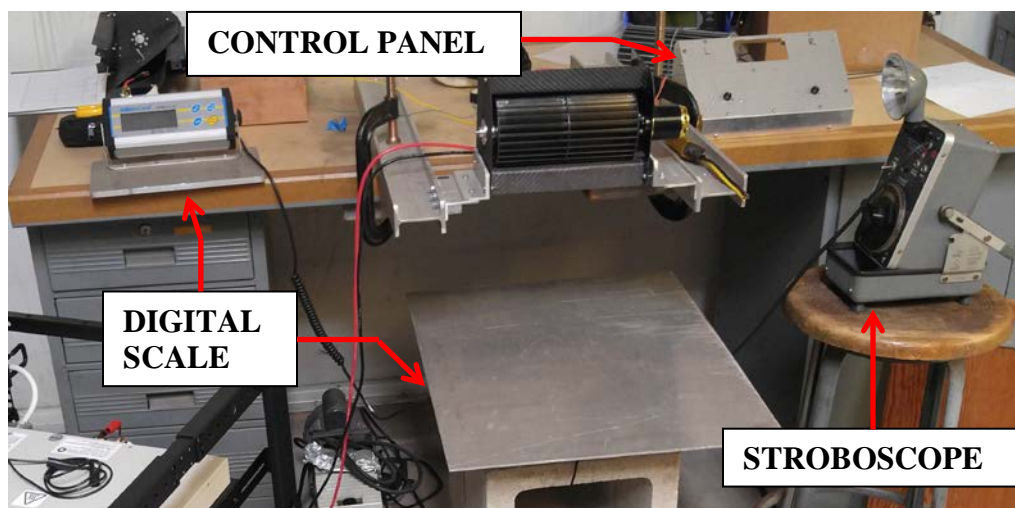


Figure 24. Full CFF thrust and power testing experimental setup.

The rotor was mounted inside the housing. The motor used was a Scorpion HKIII-4035-560KV, a brushless motor rated to a continuous 4200 W and 100 A. The motor input signal was controlled by a Scorpion Commander V 130A ESC which conditioned the DC input signal for the brushless motor. This controller was connected through a Scorpion speed control module, which in turn was connected to a simple dial switch. This allowed speed adjustment without a remote. The control panel is shown in Figure 25.

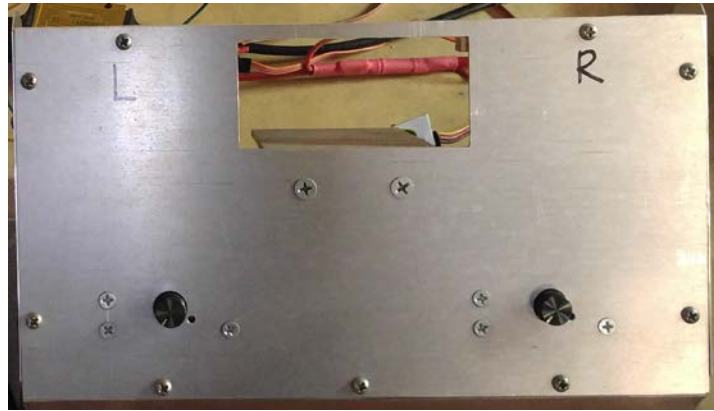


Figure 25. Control panel for manual input to CFF speed controller.

A stroboscope, shown in Figure 26, was used to measure the speed of the rotor. The light was pointed at the end of the motor. When the motor appeared to be static under the strobe light, the speed of the motor and the frequency of the strobe light were aligned, thus determining rotational speed.



Figure 26. Stroboscope used to measure rotational speed of CFF rotor.

2. Data Acquisition

As stated before, the desired data from each test was the power absorbed by the motor and the thrust output of the rotor. The power absorbed by the rotor was calculated by measuring the current output and voltage of the battery. The thrust was directly measured by using an electronic balance.

The current was measured by an ammeter coming from the battery. The electronic speed controller converts the DC signal from the motor to AC in order to power the brushless motor. Thus, the current was measured directly after the battery. Before and after each run, the battery voltage was recorded. The batteries used to power the motor, shown in Figure 27, were lithium-polymer and rated for 5,000 mAh.



Figure 27. Clamp ammeter measuring current to motor from battery.

The thrust was measured directly by placing an electronic balance beneath the outlet of the fan. A plate was placed atop the scale to ensure that the force of the entire exhaust jet was absorbed. The resolution of this balance was 5 grams. Figure 28 shows the balance with plate on top.



Figure 28. Electronic balance used to measure CFF thrust.

THIS PAGE INTENTIONALLY LEFT BLANK

IV. RESULTS AND DISCUSSION

A. MODEL CONVERGENCE

Each simulation's convergence was monitored by CFX as the solver progressed. The program plotted mass flow in, mass flow out, the difference between the two, and the torque on the rotor blades at each time step. The goal for each simulation was to have the rotor reach quasi-steady state operation. When this oscillatory state was reached, the mass flows and torque ceased to undergo significant changes. Figure 29 shows the simulation monitor output.

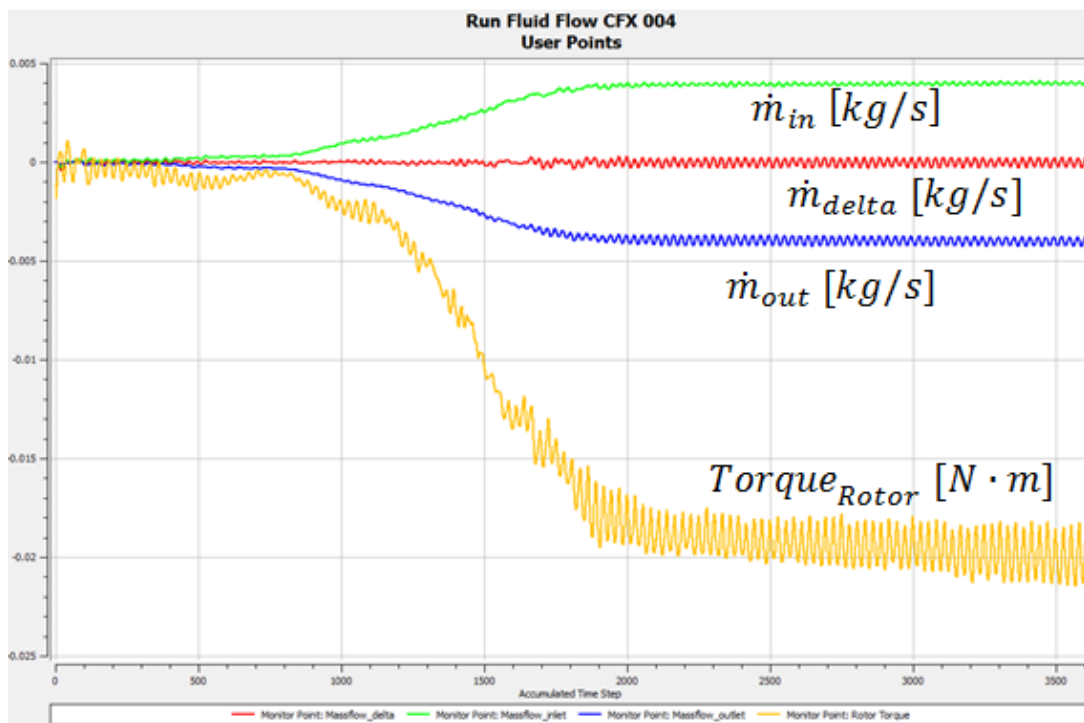


Figure 29. Mass flows and rotor torque over simulation duration for baseline model simulation at 8,000 rpm.

As first demonstrated by Martin [6] and repeated here for the baseline model, the mass flows and rotor torque reach steady values at around 1,800 time steps, equivalent at 8,000 rpm to 0.01872 s and 2.496 rotor rotations. Each simulation was ensured to have run a sufficient time for convergence, using these four monitor points as criteria.

B. FLOW VISUALIZATION

To ensure further accuracy of simulation results, the flow patterns for each run were visually examined. Both the velocity streamlines, shown in Figure 30, and the pressure field, shown in Figure 31, were plotted for each simulation. The flow patterns shown are at 0.5 mm through the 1 mm thick domain.

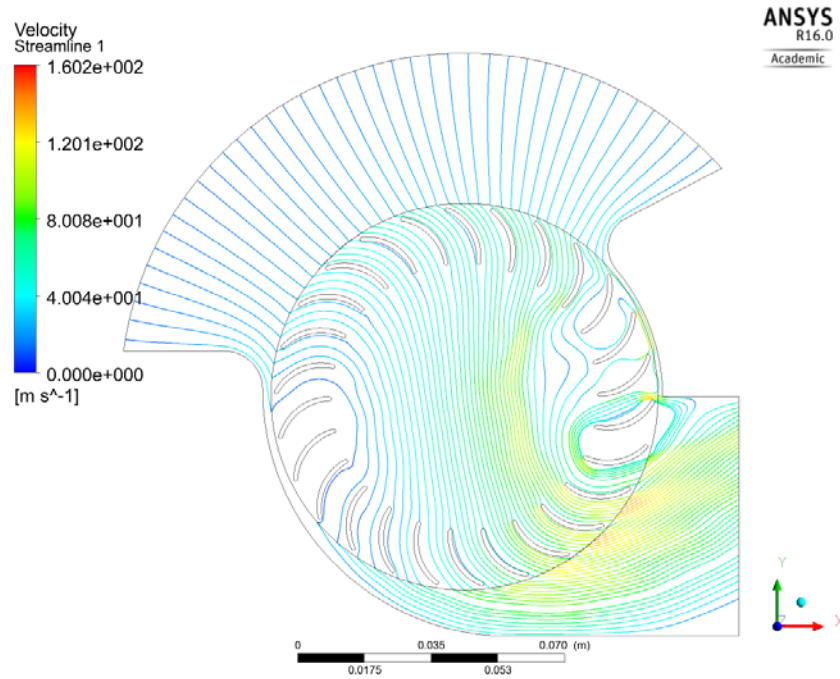


Figure 30. Baseline model velocity streamlines at 8,000 rpm.

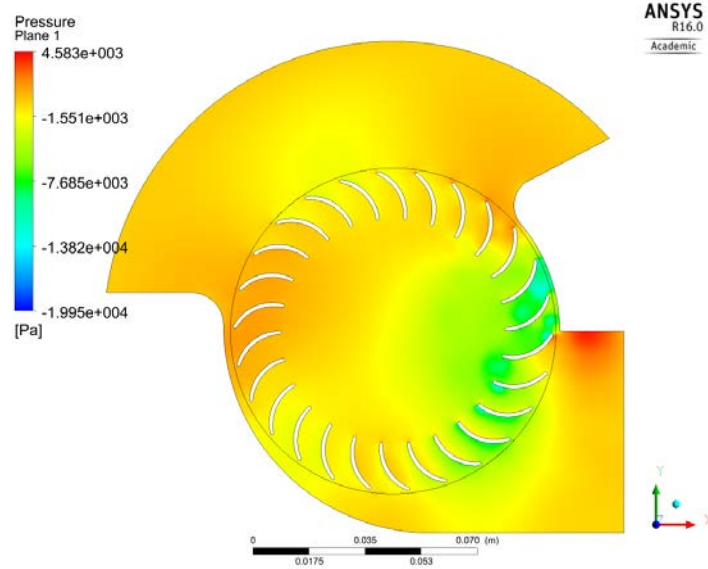


Figure 31. Baseline model pressure field at 8,000 rpm.

The velocity streamlines show that the flow is directed through an area of high velocity in the center of the fan. Additionally, the streamlines converge in the center of the rotor as the air accelerates through, and diverge as they reach the outlet and exhaust into the free stream. This suggests that in order to increase the velocity output of the rotor, the rotor must first entrain more air, then force that greater amount of streamlines to converge to the same size column in the center of the fan. This is corroborated by the areas of low pressure in Figure 31 which correlate with the areas of greatest velocity.

The other side of the rotor again sees the flow, but in the reverse direction. For this reason, double circular arc blades are a natural profile choice, because the blade experiences flow in either direction. As shown in the velocity contours, the flow must re-attach to the blades as it exits the rotor. Changing the stagger angle was chosen to be the first variable to examine in design studies, as a different stagger angle could both entrain more flow at the rotor entrance and keep the flow attached to the blades for longer as it exits the rotor. If the blade shape were changed, the exhaust flow characteristics would change in a less predictable manner than the current double-circular arc profiles. For this reason, the variable changed in the design studies was the stagger angle and not the blade shape.

C. DESIGN STUDY RESULTS

1. Thrust

The thrust was calculated using Equation (1)

$$Thrust = \dot{m}_{ave} * (V_{out} - V_{in}) \quad (1)$$

where \dot{m}_{ave} is the average mass flow across inlet and outlet, and V_{in} and V_{out} are the mass-flow averaged inlet and outlet velocities, respectively. In each simulation, the rotor and housing were stationary, equivalent to a test stand. Therefore, the free stream V_{∞} was assumed to be zero. The outlet velocity was obtained from CFX's function calculator and is the mass-flow averaged value over the entire outlet region. Despite satisfying the continuity equation, the simulation at any given time step did not have exactly equal inlet and outlet mass flows. This was most likely due to the combination of compressible flow effects and a slight domain mismatch between the sliding mesh of the rotor and the housing. Because the nodes do not join exactly between the meshes, the program had to average values between nodes, leading to slight errors in mass flow. The absolute value of the mass flows was averaged, and then used to calculate the thrust. Because a 1mm thick computational domain produced extremely small numbers, thrust values were linearly scaled to a 1 m long rotor, assuming that the flow was perfectly 2D over the whole length of the rotor. Figure 32 shows the thrust as a function of blade stagger angle.

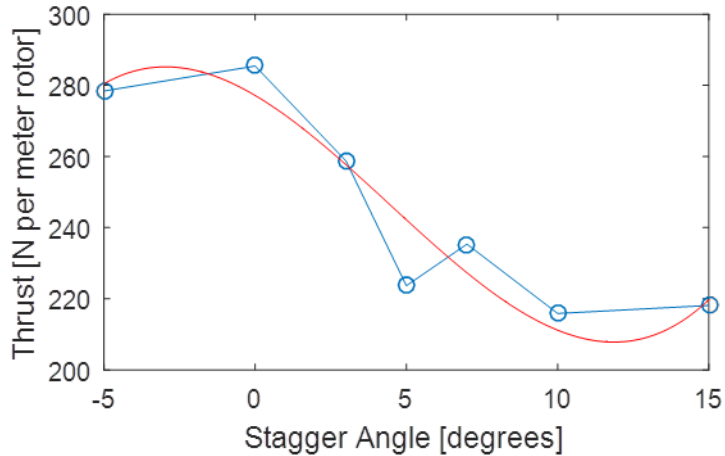


Figure 32. Thrust as a function of stagger angle.

A third-order polynomial fit was used to show the trend of thrust with stagger angle. As the stagger angle is increased, thrust generally decreases. The original stagger angle produced the greatest amount of thrust.

2. Power

The power was calculated with Equation (2).

$$Power = T_{ave} * \omega \quad (2)$$

Where T_{ave} is torque and ω is the rotational velocity of the rotor. As shown in Figure 29, the torque steadied out but did not stay at a constant value. Thus, the average value over the last 600 time steps was used, correlating to the steady oscillatory region. The rotational speed for each simulation was 8,000 rpm. As with the thrust, the power values were linearly scaled to a 1 m long rotor. Figure 33 shows the power as a function of blade angle.

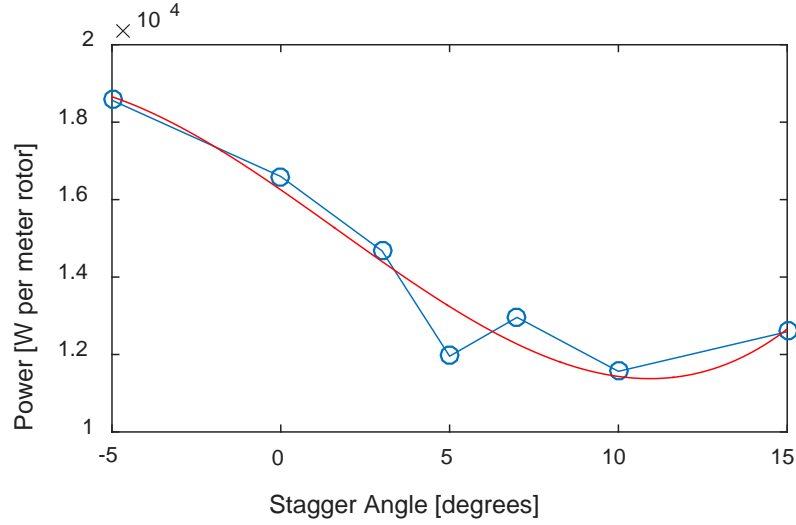


Figure 33. Power as a function of stagger angle.

The power also decreases with increasing stagger angle, as shown by the cubic fit. The highest power absorbed by the rotor was at minus 5° stagger angle.

3. Efficiency

The isentropic efficiency of each geometry was calculated using Equation (3)

$$\eta = \frac{\pi^{\frac{\gamma-1}{\gamma}} - 1}{\tau - 1} \quad (3)$$

where π is the total pressure ratio, τ is the total temperature ratio, and γ is the specific heat ratio. The specific heat ratio was taken to be 1.4, as specified in the computational model input file. The pressure and temperature ratio were calculated using mass-averaged total pressure and total temperature values at the inlet and outlet regions in CFX. Figure 34 shows the efficiencies as a function of stagger angle.

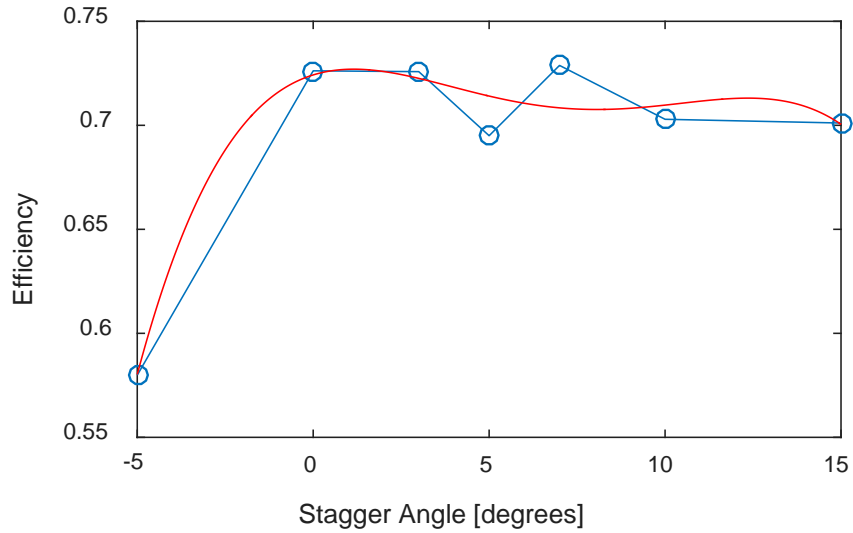


Figure 34. Isentropic efficiency as a function of stagger angle.

With the exclusion of the minus 5° simulation, each geometry had a similar isentropic efficiency, shown by the 4th order fit.

The thrust-to-power ratio for each simulation was also calculated using the thrust and power data from Figures 32 and Figure 33 respectively. Figure 35 shows the thrust-to-power ratio as a function of stagger angle.

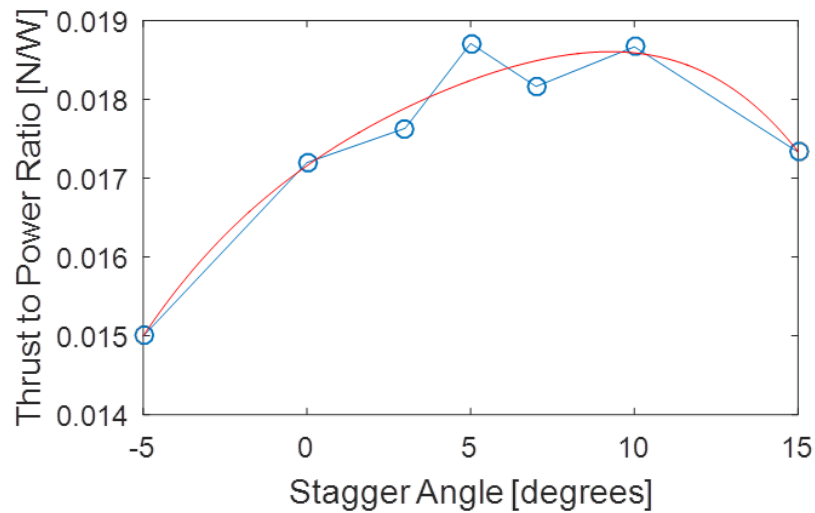


Figure 35. Thrust-to-power ratio as a function of stagger angle.

As stagger angle increased, the thrust-to-power ratio increased, until plus 10° stagger angle, as shown by the 4th order fit. Despite decreases in both thrust and power, the predictions showed that the rotor was more efficient at that stagger angle.

D. COMPARISON OF EXPERIMENTAL RESULTS FOR EXISTING DESIGN AND 3D PRINTED DESIGN

Test runs were conducted from 3,000 to 8,000 rpm. Existing data on the current rotor design were taken from Martin [6]. This data was supplemented and corroborated by repeating Martin's test on the existing rotor. Due to variability in battery conditions, tests were repeated at least three times to obtain an average value at each rotor speed for both power and thrust. When repeating Martin's testing on the existing rotor design, the propulsion components, i.e., motor, speed controller, battery, and wiring, were unable to spin the motor past 7,300 rpm. The peak power output of the battery briefly reached 4 kW before falling extremely rapidly. It is possible that any or all of the propulsion components were limiting the motor performance. The wiring, though 10 gauge, reached high temperatures, as the battery's peak current output was 160 A. The speed controller most likely cut off the current at this point, as it is only designed to work at a maximum of 130 A. For these reasons, the maximum speed of usable data for the existing rotor was 7,300 rpm.

1. Thrust

Figure 36 shows the comparison of thrust with rotor speed for the fabricated and 3D printed rotors.

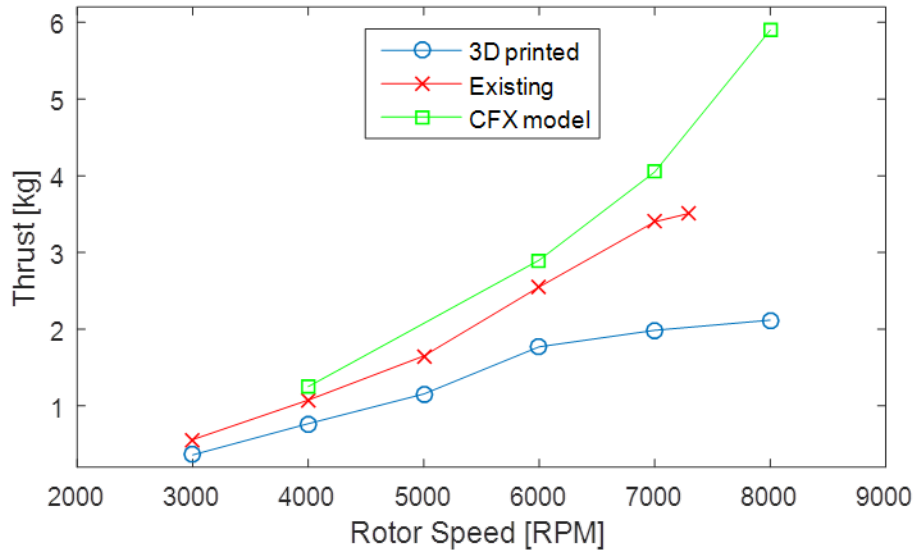


Figure 36. Thrust output of existing and 3D printed CFF rotor. Some CFX model data from Martin [6].

The thrust output of the 3D printed rotor matched a quadratic trend until 6,000 rpm. The existing rotor followed a quadratic curve until 7,000 rpm. At 7,300 rpm, the thrust decreased from the trend. For both rotors, it is possible that at higher speeds, blade tip Reynolds numbers reached sufficiently high values to trigger separation. This effect is difficult to quantify, as blades in a cross-flow fan experience flow in one direction at the inlet of the rotor and then again in the reverse direction at the outlet. Additionally, the rotor blade moves in an arc through the fluid. In order to fully experimentally quantify this effect, both rotors should be tested at higher speeds.

2. Power

Figure 37 shows the trend of power with rotor speed.

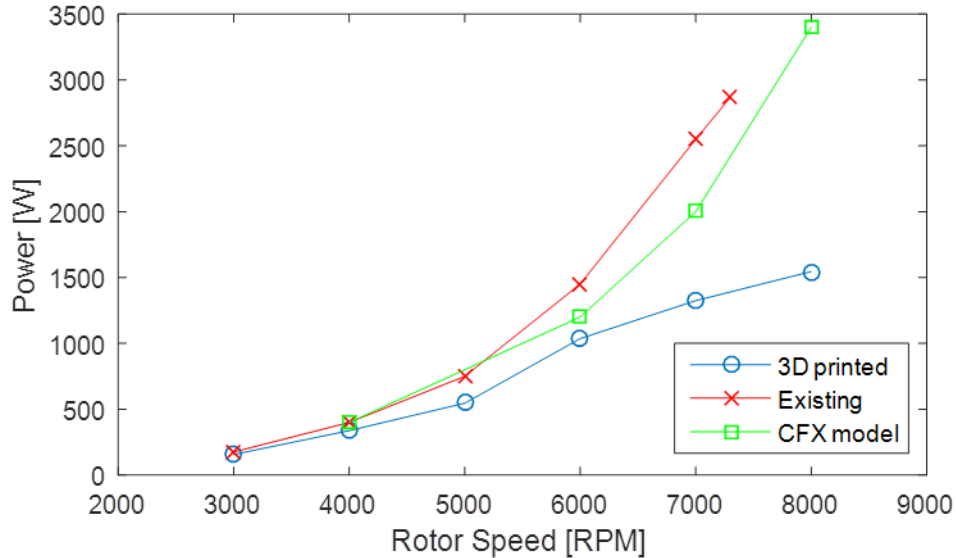


Figure 37. Power output of existing and 3D printed CFF rotor. Some CFX model data from Martin [6].

The 3D printed rotor experienced a drop in power required around 6,000 rpm. The power draw of the existing rotor followed an increasing polynomial trend. The change in power drawn by the 3D printed rotor at 6,000 rpm is further evidence that the flow characteristics of the rotor changed at this speed, and possibly began to experience high Reynolds number effects. This power drop was not observed in the existing rotor. This may have been due to the difference between the theoretical 3D printed geometry and the blade shape actually printed, discussed in the following section.

3. Thrust-to-Power Ratio

Figure 38 shows the thrust-to-power ratio for the 3D printed and existing rotors as well as CFX predictions from Martin.

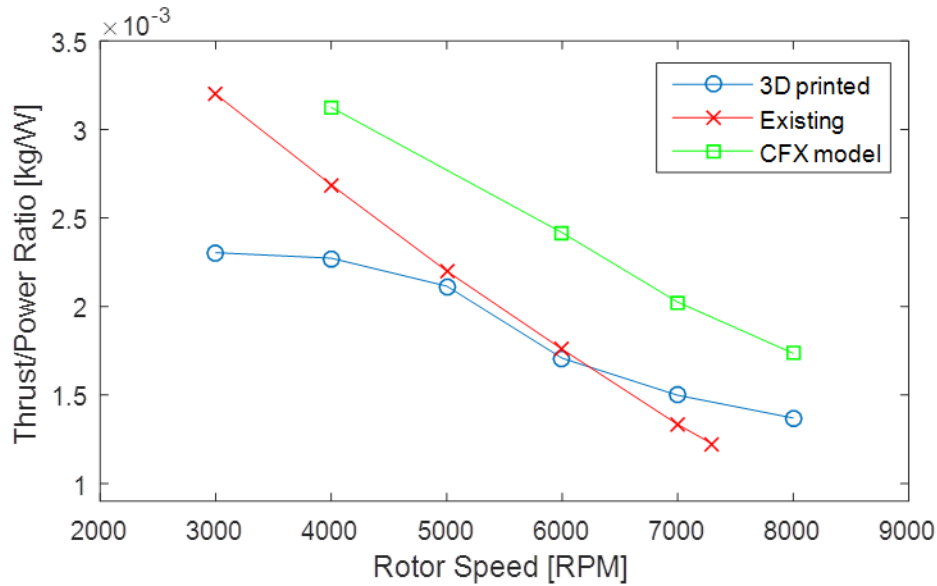


Figure 38. Thrust-to-power ratio for existing and 3D printed CFF rotors. CFX model data from Martin [6].

The thrust-to-power ratio for the existing rotor followed a negative near-linear trend. The 3D printed rotor followed a cubic polynomial trend, with a point of inflection around 6,000 rpm. The thrust-to-power ratio of mid-range speeds was similar for both rotors. At high speeds, the 3D printed rotor showed a better thrust-to-power ratio than the existing rotor. Though the thrust decreased at these speeds, the rotor operated more efficiently with respect to power consumption.

E. 3D PRINTING LIMITATIONS

Several aspects of the 3D manufacturing methods could be improved. First, it is possible that the 3D printed blade surface condition affected the flow, especially at higher speeds. Figure 39 shows the pressure surface of a 3D printed blade of the same type used in the rotor.

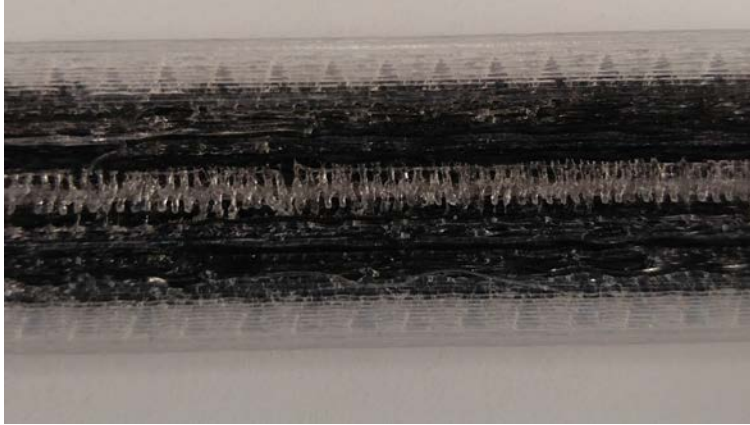


Figure 39. Surface roughness on the pressure side of 3D printed rotor blade.

Figure 40 shows the profile of the actual printed blade overlaid on the profile of the printer input file.

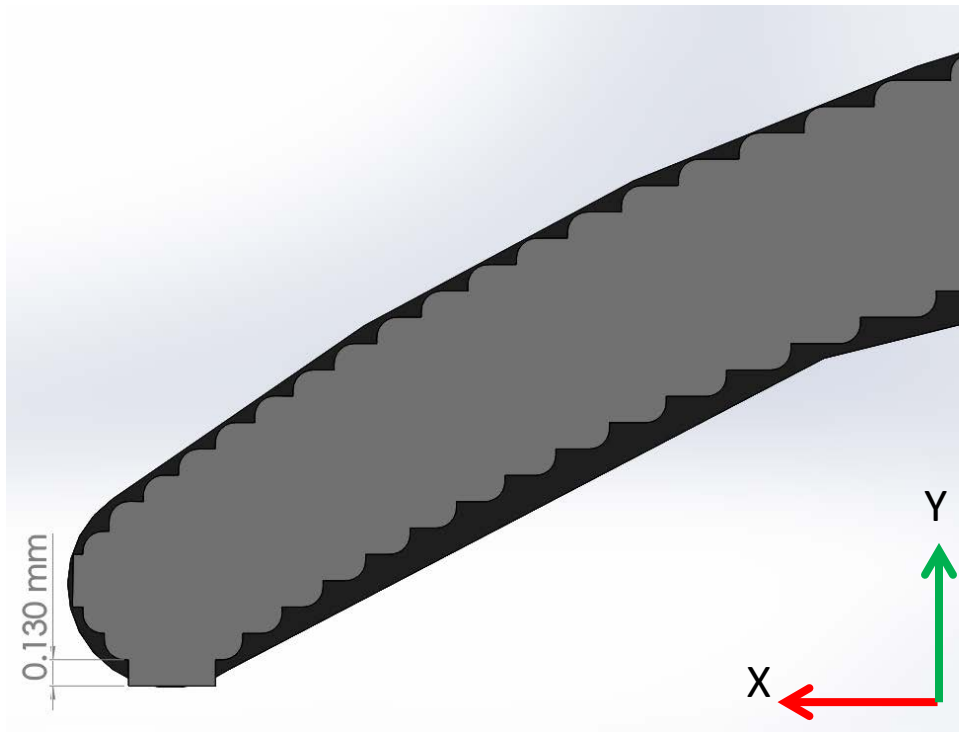


Figure 40. Schematic of printed blade profile overlaid on profile of printer input file.

The rough surface condition may have tripped turbulent flow over the blades, resulting in high drag and a subsequent drop off in thrust. The real, printed blade shape may also have affected the performance of the rotor. Printing a small, round leading and trailing edge on the blade produced a square blade instead. The limitation of the printer to layers of a finite width precluded very small round shapes, which in this case mostly came into play on the bottom of the blade. Because the print bed was flat, the printer produced a flat-bottomed blade. This flat edge of the blade may also be responsible for tripping the flow into a higher Reynolds number regime. Additionally, at higher speeds, the rotor blades flexed outwards due to high centripetal force. At this point it began to behave as a different rotor, because the incident flow angle of the flow entering the rotor and leaving the other side changed. This could also account for the changes in performance.

In the future, 3D printing methods could be used to implement innovative blade shapes. For example, serrating the trailing edge of compressor blades has been shown to produce less noise [9]. Serrating the edges of the cross-flow fan blades could produce the same effect. Additionally, as noted previously, the blades of the 3D printed rotor bowed out radially at higher speeds. 3D printing concave blades could counter this effect.

Lastly, the design changes recommended by the conclusions of the blade stagger angle study should be implemented in a new CFF rotor. Testing this design using the experimental apparatus in this study would provide validation to the ANSYS-CFX model, and could produce additional design change recommendation. Furthermore, this rotor could be manufactured using both 3D printing and traditional methods, allowing a comparison of the optimized design as well.

THIS PAGE INTENTIONALLY LEFT BLANK

V. CONCLUSIONS

A. OPTIMUM STAGGER ANGLE

Part of this study's objective was to improve the performance of the current cross-flow fan rotor by varying the blade stagger angle. As stagger angle increased, both thrust and power consumption decreased until a 10° forward stagger. At 7° to 10° forward stagger angle, a maximum thrust-to-power ratio was reached. For flight efficiency, especially a UAV design with limited battery life, thrust-to-power ratio is crucial for extending flight times. For this reason, moving the stagger angle of the blades forward by 7° to 10° will improve the CFF rotor. However, if the UAV requires more thrust, the stagger angle of the blades should not be changed, as their current orientation provided the most thrust.

B. VIABILITY OF 3D PRINTED CROSS-FLOW FAN ROTOR

The second part of this study was to determine whether or not 3D printing is a viable manufacturing method for a carbon fiber CFF rotor. Although the overall thrust for the 3D printed rotor was much lower at higher speeds than that of the existing rotor, the thrust-to-power requirement was comparable at mid-range speeds. The weight of the two rotors should also be taken into account when comparing performance. Table 1 details the thrust-to-weight ratio for each rotor at maximum thrust.

Table 1. Thrust-to-weight ratio for 3D printed rotor and existing rotor.

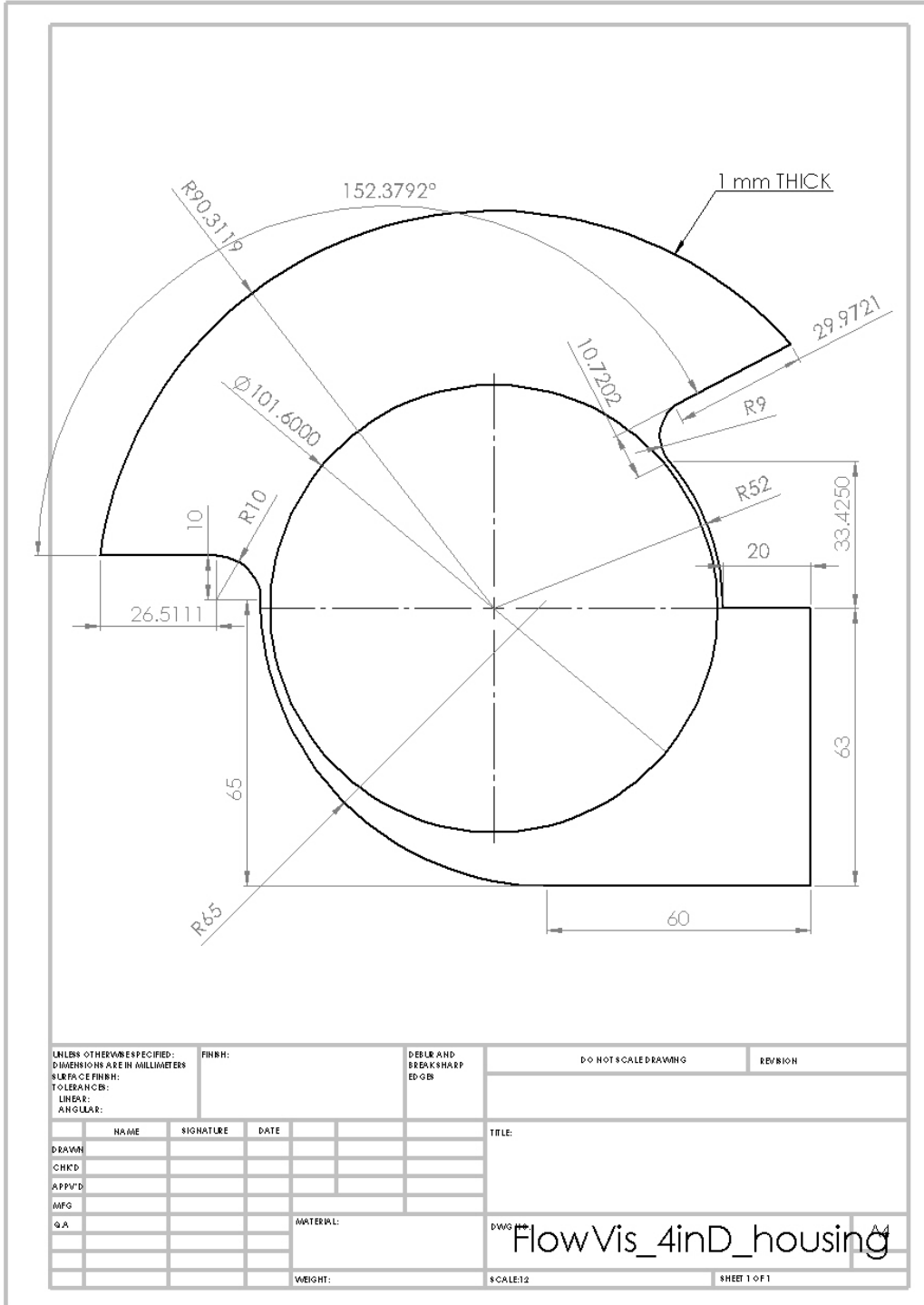
	Thrust/weight
3D Printed	12.44
Existing	16.27

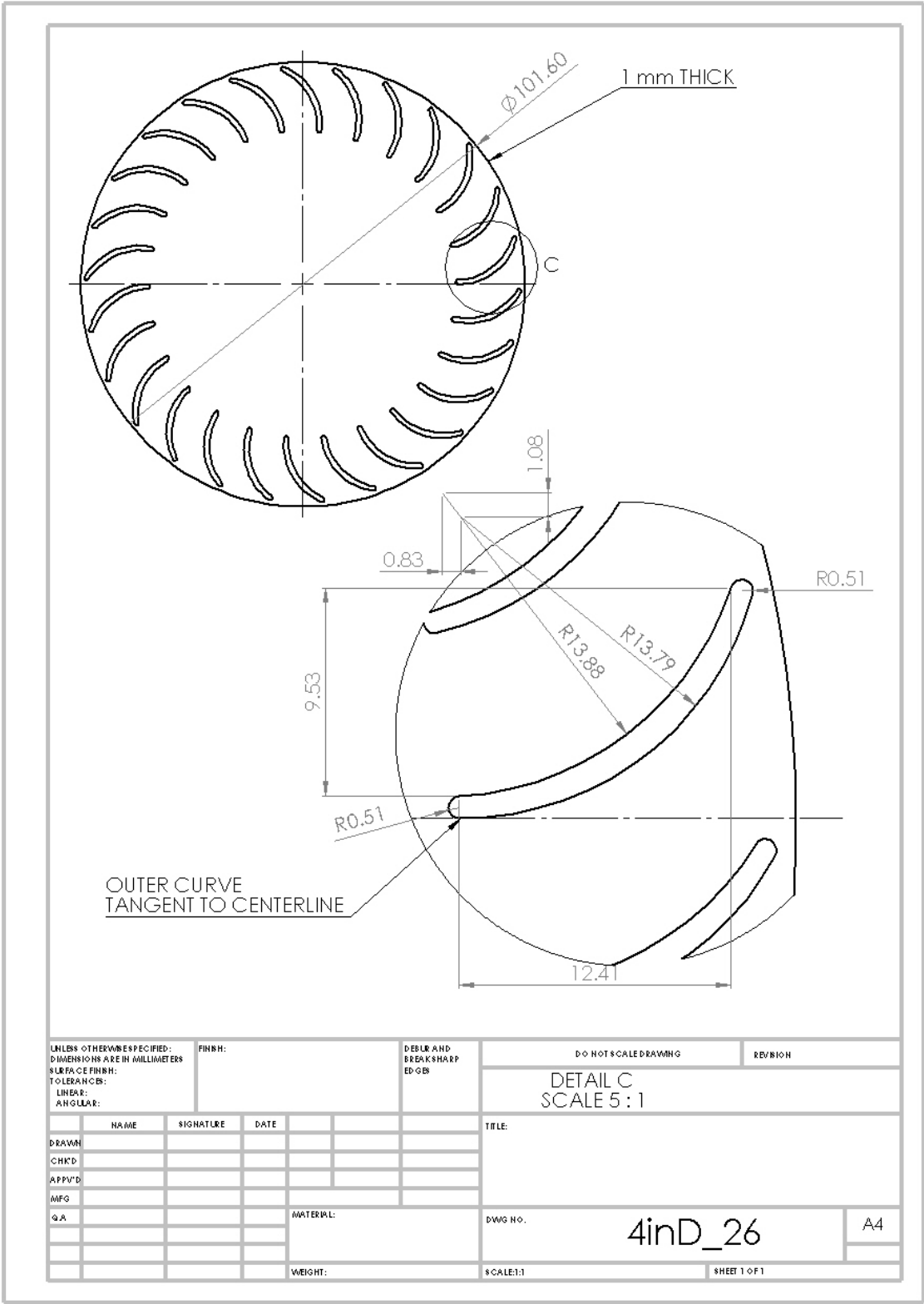
Overall, the 3D printed rotor performed as efficiently as the existing design with respect to power at mid-range speeds, but not with respect to weight. The existing rotor also produced a maximum thrust value 66% greater than that of the 3D printed rotor.

C. RECOMMENDATIONS

Further examination of CFF performance at different rotor speeds and stagger angles would be useful for design of a new rotor. The existing rotor was only able to achieve 7,300 rpm. This same rotor, using the same power system, provided propulsion for the UAV used by Fulton [10]. It is unlikely that the rotor operated at full output on this UAV at all times, and more likely that the rotor operated at speeds of 5,000–6,000 rpm. For this reason, design studies incorporating speed variations into stagger angle studies could produce a more efficient design at speeds realistic to operation of current CFF UAVs. Furthermore, when testing the existing rotor and 3D printed rotor, the drive system could not handle the power requirements. In order to fully characterize the performance of the real rotors, it is recommended that a more powerful drive system be used.

APPENDIX A. DIMENSIONED DRAWINGS OF COMPUTATIONAL DOMAINS





UNLESS OTHERWISE SPECIFIED: DIMENSIONS ARE IN MILLIMETERS		FINISH:		DEBUR AND BREAK SHARP EDGES		DO NOT SCALE DRAWING		REVISION	
SURFACE FINISH:						DETAIL C SCALE 5 : 1			
TOLERANCES:									
LINEAR:									
ANGULAR:									
	NAME	SIGNATURE	DATE			TITLE:			
DRAWN									
CHK'D									
APP'V'D									
MFG									
QA						DWG NO.		A4	
						4inD_26			
						SCALE: 1:1		SHEET 1 OF 1	
						WEIGHT:			

APPENDIX B. CFX INPUT FILE SETTINGS

LIBRARY:

CEL:

EXPRESSIONS:

thrust = massFlowAve(Pressure)@REGION:Outlet

END

END

MATERIAL: Air Ideal Gas

Material Description = Air Ideal Gas (constant Cp)

Material Group = Air Data, Calorically Perfect Ideal Gases

Option = Pure Substance

Thermodynamic State = Gas

PROPERTIES:

Option = General Material

EQUATION OF STATE:

Molar Mass = 28.96 [kg kmol⁻¹]

Option = Ideal Gas

END

SPECIFIC HEAT CAPACITY:

Option = Value

Specific Heat Capacity = 1.0044E+03 [J kg⁻¹ K⁻¹]

Specific Heat Type = Constant Pressure

END

REFERENCE STATE:

Option = Specified Point

Reference Pressure = 1 [atm]

Reference Specific Enthalpy = 0. [J/kg]

Reference Specific Entropy = 0. [J/kg/K]

Reference Temperature = 25 [C]

END

DYNAMIC VISCOSITY:

Dynamic Viscosity = 1.831E-05 [kg m⁻¹ s⁻¹]

Option = Value

END

THERMAL CONDUCTIVITY:

Option = Value

Thermal Conductivity = 2.61E-2 [W m⁻¹ K⁻¹]

END

ABSORPTION COEFFICIENT:

Absorption Coefficient = 0.01 [m⁻¹]

Option = Value

END

SCATTERING COEFFICIENT:

```

    Option = Value
    Scattering Coefficient = 0.0 [m^-1]
END
REFRACTIVE INDEX:
    Option = Value
    Refractive Index = 1.0 [m m^-1]
END
END
END
END
FLOW: Flow Analysis 1
SOLUTION UNITS:
    Angle Units = [rad]
    Length Units = [m]
    Mass Units = [kg]
    Solid Angle Units = [sr]
    Temperature Units = [K]
    Time Units = [s]
END
ANALYSIS TYPE:
    Option = Transient
EXTERNAL SOLVER COUPLING:
    Option = None
END
INITIAL TIME:
    Option = Automatic with Value
    Time = 0 [s]
END
TIME DURATION:
    Option = Total Time
    Total Time = 0.0375 [s]
END
TIME STEPS:
    Option = Timesteps
    Timesteps = 1.04e-005 [s]
END
END
DOMAIN: Housing
    Coord Frame = Coord 0
    Domain Type = Fluid
    Location = B668
BOUNDARY: HousingtoRotor Side 1
    Boundary Type = INTERFACE
    Location = HousingInterface
BOUNDARY CONDITIONS:

```

```

HEAT TRANSFER:
  Option = Conservative Interface Flux
END
MASS AND MOMENTUM:
  Option = Conservative Interface Flux
END
TURBULENCE:
  Option = Conservative Interface Flux
END
END
BOUNDARY: Inlet
Boundary Type = OPENING
Location = Inlet
BOUNDARY CONDITIONS:
FLOW DIRECTION:
  Option = Normal to Boundary Condition
END
FLOW REGIME:
  Option = Subsonic
END
HEAT TRANSFER:
  Option = Static Temperature
  Static Temperature = 288.15 [K]
END
MASS AND MOMENTUM:
  Option = Opening Pressure and Direction
  Relative Pressure = 0 [Pa]
END
TURBULENCE:
  Option = Medium Intensity and Eddy Viscosity Ratio
END
END
BOUNDARY: Outlet
Boundary Type = OUTLET
Location = Outlet
BOUNDARY CONDITIONS:
FLOW REGIME:
  Option = Subsonic
END
MASS AND MOMENTUM:
  Option = Average Static Pressure
  Pressure Profile Blend = 0.05
  Relative Pressure = 0 [Pa]

```



```
END
PRESSURE AVERAGING:
  Option = Average Over Whole Outlet
END
END
END
BOUNDARY: Stator_Walls
  Boundary Type = WALL
  Location = HousingWalls
BOUNDARY CONDITIONS:
  HEAT TRANSFER:
    Option = Adiabatic
  END
  MASS AND MOMENTUM:
    Option = No Slip Wall
  END
  WALL ROUGHNESS:
    Option = Smooth Wall
  END
END
END
BOUNDARY: Symmetry1
  Boundary Type = SYMMETRY
  Location = sym1,sym2
END
DOMAIN MODELS:
  BUOYANCY MODEL:
    Option = Non Buoyant
  END
  DOMAIN MOTION:
    Option = Stationary
  END
  MESH DEFORMATION:
    Option = None
  END
  REFERENCE PRESSURE:
    Reference Pressure = 1 [atm]
  END
END
FLUID DEFINITION: Fluid 1
  Material = Air Ideal Gas
  Option = Material Library
MORPHOLOGY:
  Option = Continuous Fluid
END
```

END
 FLUID MODELS:
 COMBUSTION MODEL:
 Option = None
 END
 HEAT TRANSFER MODEL:
 Include Viscous Work Term = On
 Option = Total Energy
 END
 THERMAL RADIATION MODEL:
 Option = None
 END
 TURBULENCE MODEL:
 Option = k epsilon
 END
 TURBULENT WALL FUNCTIONS:
 High Speed Model = Off
 Option = Scalable
 END
 END
 INITIALISATION:
 Option = Automatic
 INITIAL CONDITIONS:
 Velocity Type = Cylindrical
 CYLINDRICAL VELOCITY COMPONENTS:
 Option = Automatic with Value
 Velocity Axial Component = 0 [m s⁻¹]
 Velocity Theta Component = 0 [m s⁻¹]
 Velocity r Component = 0 [m s⁻¹]
 AXIS DEFINITION:
 Option = Coordinate Axis
 Rotation Axis = Coord 0.3
 END
 END
 STATIC PRESSURE:
 Option = Automatic with Value
 Relative Pressure = 0 [Pa]
 END
 TEMPERATURE:
 Option = Automatic with Value
 Temperature = 288.15 [K]
 END
 TURBULENCE INITIAL CONDITIONS:
 Option = Medium Intensity and Eddy Viscosity Ratio
 END

```

END
END
END
DOMAIN: Rotor
  Coord Frame = Coord 0
  Domain Type = Fluid
  Location = B379
  BOUNDARY: HousingtoRotor Side 2
    Boundary Type = INTERFACE
    Location = RotorInterface
    BOUNDARY CONDITIONS:
      HEAT TRANSFER:
        Option = Conservative Interface Flux
      END
      MASS AND MOMENTUM:
        Option = Conservative Interface Flux
      END
      TURBULENCE:
        Option = Conservative Interface Flux
      END
    END
  END
END
BOUNDARY: Rotor_Blades
  Boundary Type = WALL
  Frame Type = Rotating
  Location = \
    F320.379,F321.379,F322.379,F323.379,F324.379,F325.379,F326.379,F327.3\
    79,F328.379,F329.379,F330.379,F331.379,F332.379,F333.379,F334.379,F33\
    5.379,F336.379,F337.379,F338.379,F339.379,F340.379,F341.379,F342.379,\
    F343.379,F344.379,F345.379,F346.379,F347.379,F348.379,F349.379,F350.3\
    79,F351.379,F352.379,F353.379,F354.379,F355.379,F356.379,F357.379,F35\
    8.379,F359.379,F360.379,F361.379,F362.379,F363.379,F364.379,F365.379,\
    F366.379,F367.379,F368.379,F369.379,F370.379,F371.379,F372.379,F373.3\
    79,F374.379,F375.379,F376.379,F377.379,F378.379,F381.379,F382.379,F38\
    4.379,F385.379,F386.379,F388.379,F389.379,F390.379,F391.379,F392.379,\
    F393.379,F394.379,F395.379,F396.379,F397.379,F398.379,F399.379,F400.3\
    79,F401.379,F402.379,F403.379,F404.379,F405.379,F406.379,F407.379,F40\
    8.379,F409.379,F410.379,F411.379,F412.379,F413.379,F414.379,F415.379,\
    F416.379,F417.379,F418.379,F419.379,F420.379,F421.379,F422.379,F423.3\
    79,F424.379,F425.379,F426.379,F427.379
  BOUNDARY CONDITIONS:
    HEAT TRANSFER:
      Option = Adiabatic
    END
    MASS AND MOMENTUM:

```

```

    Option = No Slip Wall
END
WALL ROUGHNESS:
    Option = Smooth Wall
END
END
BOUNDARY: Symmetry
    Boundary Type = SYMMETRY
    Location = sym3,sym4
END
DOMAIN MODELS:
    BUOYANCY MODEL:
        Option = Non Buoyant
    END
    DOMAIN MOTION:
        Angular Velocity = 8000 [rev min^-1]
        Option = Rotating
    AXIS DEFINITION:
        Option = Coordinate Axis
        Rotation Axis = Coord 0.3
    END
END
MESH DEFORMATION:
    Option = None
END
REFERENCE PRESSURE:
    Reference Pressure = 1 [atm]
END
END
FLUID DEFINITION: Fluid 1
    Material = Air Ideal Gas
    Option = Material Library
MORPHOLOGY:
    Option = Continuous Fluid
END
END
FLUID MODELS:
    COMBUSTION MODEL:
        Option = None
    END
    HEAT TRANSFER MODEL:
        Include Viscous Work Term = On
        Option = Total Energy
    END
END

```

```

THERMAL RADIATION MODEL:
  Option = None
END
TURBULENCE MODEL:
  Option = k epsilon
END
TURBULENT WALL FUNCTIONS:
  High Speed Model = Off
  Option = Scalable
END
END
INITIALISATION:
  Frame Type = Rotating
  Option = Automatic
INITIAL CONDITIONS:
  Velocity Type = Cylindrical
CYLINDRICAL VELOCITY COMPONENTS:
  Option = Automatic with Value
  Velocity Axial Component = 0 [m s^-1]
  Velocity Theta Component = 0 [m s^-1]
  Velocity r Component = 0 [m s^-1]
END
STATIC PRESSURE:
  Option = Automatic with Value
  Relative Pressure = 0 [Pa]
END
TEMPERATURE:
  Option = Automatic with Value
  Temperature = 288.15 [K]
END
TURBULENCE INITIAL CONDITIONS:
  Option = Medium Intensity and Eddy Viscosity Ratio
END
END
END
END
DOMAIN INTERFACE: HousingtoRotor
  Boundary List1 = HousingtoRotor Side 1
  Boundary List2 = HousingtoRotor Side 2
  Interface Type = Fluid Fluid
INTERFACE MODELS:
  Option = General Connection
FRAME CHANGE:
  Option = Transient Rotor Stator
END

```

```

MASS AND MOMENTUM:
  Option = Conservative Interface Flux
MOMENTUM INTERFACE MODEL:
  Option = None
END
END
PITCH CHANGE:
  Option = Automatic
END
END
MESH CONNECTION:
  Option = GGI
END
END
OUTPUT CONTROL:
MONITOR OBJECTS:
MONITOR BALANCES:
  Option = Full
END
MONITOR FORCES:
  Option = Full
END
MONITOR PARTICLES:
  Option = Full
END
MONITOR POINT: Massflow_delta
  Coord Frame = Coord 0
  Expression Value = massFlow()@Inlet+massFlow()@Outlet
  Option = Expression
END
MONITOR POINT: Massflow_inlet
  Coord Frame = Coord 0
  Expression Value = massFlow()@Inlet
  Option = Expression
END
MONITOR POINT: Massflow_outlet
  Coord Frame = Coord 0
  Expression Value = massFlow()@Outlet
  Option = Expression
END
MONITOR POINT: Rotor Torque
  Coord Frame = Coord 0
  Expression Value = torque_z()@Rotor_Blades
  Option = Expression
END

```

```

MONITOR RESIDUALS:
  Option = Full
END
MONITOR TOTALS:
  Option = Full
END
RESULTS:
  File Compression Level = Default
  Option = Standard
END
TRANSIENT RESULTS: Transient Results 1
  File Compression Level = Default
  Option = Standard
OUTPUT FREQUENCY:
  Option = Timestep Interval
  Timestep Interval = 25
END
END
END
SOLVER CONTROL:
  Turbulence Numerics = First Order
ADVECTION SCHEME:
  Option = High Resolution
END
COMPRESSIBILITY CONTROL:
  High Speed Numerics = On
END
CONVERGENCE CONTROL:
  Maximum Number of Coefficient Loops = 5
  Minimum Number of Coefficient Loops = 1
  Timescale Control = Coefficient Loops
END
CONVERGENCE CRITERIA:
  Residual Target = 1.E-4
  Residual Type = RMS
END
TRANSIENT SCHEME:
  Option = Second Order Backward Euler
TIMESTEP INITIALISATION:
  Option = Automatic
END
END
END
END

```

```

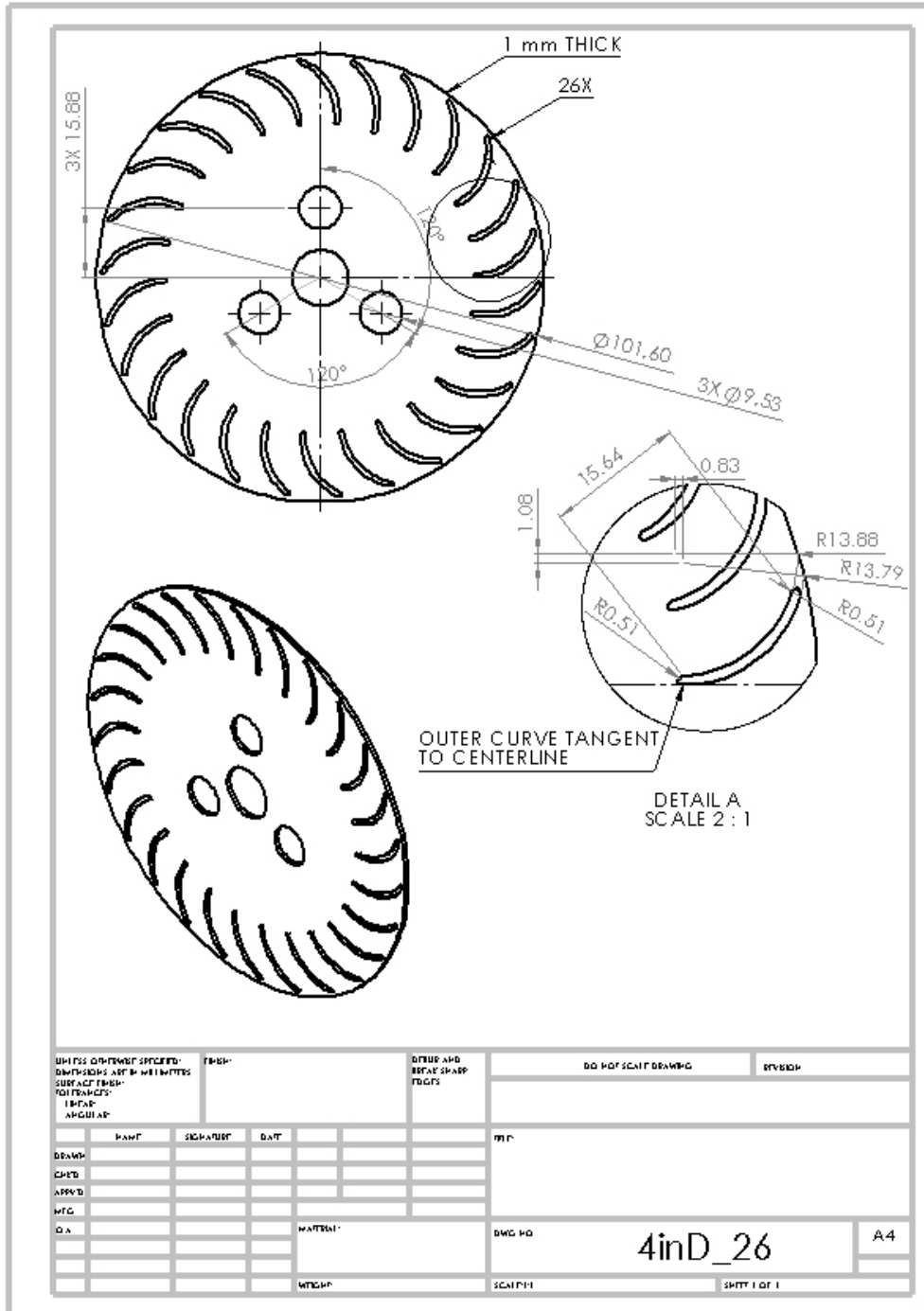
COMMAND FILE:
  Version = 16.0
  Results Version = 16.0
END
SIMULATION CONTROL:
EXECUTION CONTROL:
  EXECUTABLE SELECTION:
    Double Precision = Yes
  END
INTERPOLATOR STEP CONTROL:
  Runtime Priority = Standard
DOMAIN SEARCH CONTROL:
  Bounding Box Tolerance = 0.01
  END
INTERPOLATION MODEL CONTROL:
  Enforce Strict Name Mapping for Phases = Off
  Mesh Deformation Option = Automatic
  Particle Relocalisation Tolerance = 0.01
  END
MEMORY CONTROL:
  Memory Allocation Factor = 1.5
  END
END
PARALLEL HOST LIBRARY:
  HOST DEFINITION: marine
    Host Architecture String = winnt-amd64
    Installation Root = C:\Program Files\ANSYS Inc\v%v\CFX
  END
  END
PARTITIONER STEP CONTROL:
  Multidomain Option = Independent Partitioning
  Runtime Priority = Standard
EXECUTABLE SELECTION:
  Use Large Problem Partitioner = Off
  END
MEMORY CONTROL:
  Memory Allocation Factor = 1.5
  END
PARTITION SMOOTHING:
  Maximum Partition Smoothing Sweeps = 100
  Option = Smooth
  END
PARTITIONING TYPE:
  MeTiS Type = k-way
  Option = MeTiS

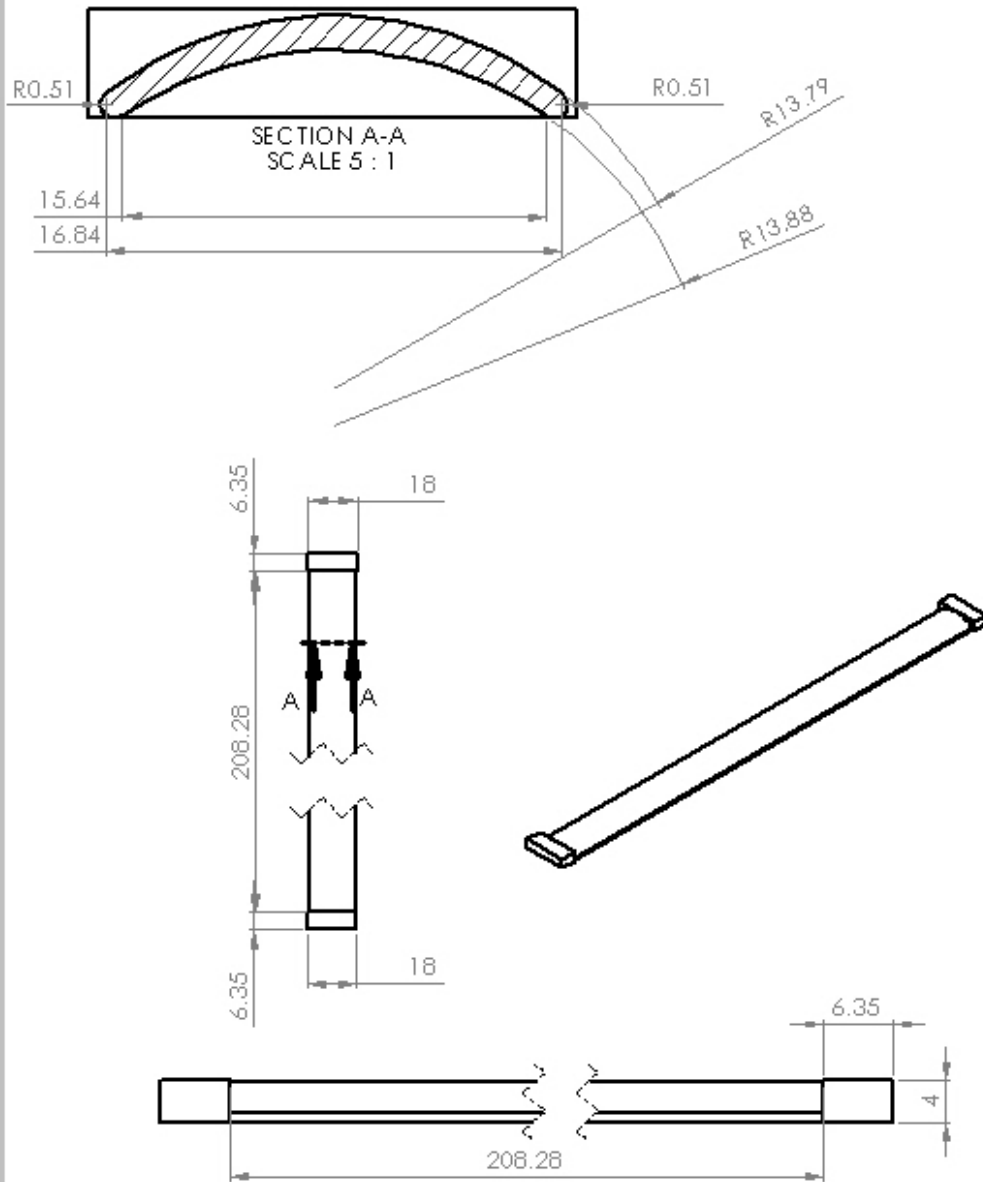
```



```
Partition Size Rule = Automatic
Partition Weight Factors = 0.12500, 0.12500, 0.12500, 0.12500, \
  0.12500, 0.12500, 0.12500, 0.12500
END
END
RUN DEFINITION:
Run Mode = Full
Solver Input File = Fluid Flow CFX.def
Solver Results File = C:/Waterman/CFD/Design \
  Studies/Baseline_model_performance_pending/dp0_CFX_Solution/Fluid \
  Flow CFX_004.res
END
SOLVER STEP CONTROL:
Runtime Priority = Standard
MEMORY CONTROL:
Memory Allocation Factor = 1.5
END
PARALLEL ENVIRONMENT:
Number of Processes = 8
Start Method = Platform MPI Local Parallel
Parallel Host List = marine*8
END
END
END
END
```

APPENDIX C. DIMENSIONED DRAWINGS OF 3D PRINTER INPUT FILES





UNLESS OTHERWISE SPECIFIED: DIMENSIONS ARE IN MILLIMETERS SURFACE FINISH: FOR FRAMES: TEXTURE ANGULAR	FINISH			DRESS AND BEFORE SHARP EDGES	DO NOT SCALE DRAWING	REVISION
	DATE				DATE	
DRAWN	SIGNATURE	DATE			M.P.	
CHECKED						
APPROVED						
WTC						
Q.A.				MATERIAL	DWG. NO. Current_blades_8plus_1n A4	
				WEIGHT	SCALE	SHEET 1 OF 1

LIST OF REFERENCES

- [1] P. L. Mortier, "Fan or blowing apparatus." U.S. Patent 507445, 1893.
- [2] W. F. Foshag and G. D. Boehler, "Review and preliminary evaluation of lifting horizontal-axis rotating-wing aeronautical systems (HARWAS)," Aerophysics Company, Washington, DC, 1969.
- [3] "Multi-bypass ratio propulsion system technology development," LTV Aerospace Corporation, Naval Air System Command contract N00019-74-C-0434, 24 July 1975.
- [4] G. J. Harloff and D. R. Wilson, "Cross-flow propulsion fan experimental development and finite-element modeling," *AIAA*, vol. 18, no. 4, pp. 310–317, April 1981.
- [5] A. M. Jones, "Integration of twenty-bladed cross-flow fan into vertical take-off and landing aircraft," M.S. thesis, Dept. Mech. Aero. Eng., Naval Postgrad. School, Monterey, CA, 2013.
- [6] M. J. Martin, "Development of a cross-flow fan rotor for vertical take-off and landing aircraft," M.S. thesis, Dept. Mech. Aero. Eng., Naval Postgrad. School, Monterey, CA, 2013.
- [7] E. D. Smitley, "Development of a cross-flow fan powered quad-rotor unmanned aerial vehicle," M.S. thesis, Dept. Mech. Aero. Eng., Naval Postgrad. School, Monterey, CA, 2015.
- [8] J. Yao, "Numerical studies of cross-flow fan for propulsion: comparison of turbulence models and blades configuration optimization," Dept. Mech. Eng., National University of Singapore, Singapore, 2014.
- [9] A. Borgoltz, "Modifications of coherent structures in fan blade wakes for broadband noise reduction," Ph.D. dissertation, Virginia Polytechnic Institute, Blacksburg, VA, 2007.
- [10] J. Fulton, "Wing-embedded, cross-flow fan, vertical take off and landing air vehicle," M.S. thesis, Dept. Mech. Aero. Eng., Naval Postgrad. School, Monterey, CA, 2016.

THIS PAGE INTENTIONALLY LEFT BLANK

INITIAL DISTRIBUTION LIST

1. Defense Technical Information Center
Ft. Belvoir, Virginia
2. Dudley Knox Library
Naval Postgraduate School
Monterey, California